JGR Biogeosciences

RESEARCH ARTICLE
10.1029/2019JG005419

Shale as a Source of Organic Carbon in Floodplain Sediments of a Mountainous Watershed

Patricia M. Fox[1], Markus Bill[1], Katherine Heckman[2], Mark Conrad[1], Carolyn Anderson[3], Marco Keiluweit[3], and Peter S. Nico[1]

[1]Earth and Environmental Sciences Area, Lawrence Berkeley National Laboratory, Berkeley, CA, USA, [2]Northern Research Station, USDA-Forest Service, Madison, WI, USA, [3]School of Earth & Sustainability; Stockbridge School of Agriculture, University of Massachusetts Amherst, Amherst, MA, USA

Key Points:
- Shale-derived organic carbon (OC) accounts for an estimated 23–34% of total OC in floodplain sediments of a shale-dominated landscape
- The mineral fraction contains the largest and oldest pool of OC, and shale-derived OC is also observed in pools considered to be actively cycled
- Implications for shale as an unrecognized source of global C and other rock-derived elements and for interpretation of bulk ^{14}C data

Supporting Information:
- Supporting Information S1

Correspondence to:
P. M. Fox,
pmfox@lbl.gov

Citation:
Fox, P. M., Bill, M., Heckman, K., Conrad, M., Anderson, C., Keiluweit, M., & Nico, P. S. (2020). Shale as a source of organic carbon in floodplain sediments of a mountainous watershed. *Journal of Geophysical Research: Biogeosciences*, *125*, e2019JG005419. https://doi.org/10.1029/2019JG005419

Received 5 AUG 2019
Accepted 11 JAN 2020
Accepted article online 30 JAN 2020

Abstract Shales contain high levels of organic carbon (OC) and represent a large fraction of the Earth's reduced carbon stocks. While recent evidence suggests that shale-derived OC may be actively cycled in riverine systems, this process is poorly understood and not currently considered in global C models. Through the use of sediment density fractionations, extractions, radiocarbon measurements, and chemical characterization, we provide information on the abundance, chemistry, and mobility of shale-derived OC in floodplain sediments of a shale-rich mountainous watershed. The heavy fraction of the sediment, representing mineral-associated OC, is the largest (84 ± 6% of TOC) and oldest ($\Delta^{14}C$ values −224 to −853‰) OC pool. Evidence of shale-derived OC is observed in all sediment C pools (i.e., occluded light fraction, water-soluble, and pyrophosphate-extractable) except the free light fraction, which is entirely modern. Relatively consistent chemistry was observed across samples for extracted and density-separated OC, despite wide ranges of $\Delta^{14}C$ values. Carbon spectroscopy revealed that floodplain sediments had a higher degree of functionalized aromatic groups and lower carbonate content compared to shale collected nearby, consistent with chemical alteration and mixing with other C sources in the floodplain. We estimate that approximately 23–34% of sediment OC is derived from shale, with implications for other shale-derived elements (e.g., N). This study demonstrates the important contribution of shale-OC, particularly in environments with low litter inputs. The large impact of radiocarbon-dead shale-OC, which has a thermally altered chemical structure distinct from plant litter, on $\Delta^{14}C$ values and reactivity of sediment-OC must be considered.

Plain Language Summary Shales contain high levels of organic carbon (OC) and represent a large fraction of the Earth's total carbon stocks. While recent evidence suggests that shale-derived OC, which is millions of years old, may be actively cycled in riverine systems, this process is poorly understood and not currently considered in global C models. In this study, we analyze sediments collected from the floodplain of the East River, CO, located in a high-elevation mountainous watershed underlain by shale bedrock, to determine the importance and mobility of shale-derived OC in this environment. OC closely associated with sediment minerals is the largest (84 ± 6%) and oldest OC pool, containing a large, but variable, amount of shale-derived OC. Evidence of shale-derived OC is also observed in other sediment OC pools which are considered to be more mobile and more easily degraded to carbon dioxide by bacteria (e.g., water-soluble). This study concludes that there are two primary OC sources in floodplain sediments, plant-litter and shale-derived OC, each with distinct chemical characteristics and reactivity. We estimate that 23–34% of the sediment OC is derived from shale, demonstrating the important contribution of shale-OC to the carbon cycle at this site, particularly in environments with low plant-litter inputs.

1. Introduction

Sedimentary rocks, such as shale, can contain high levels of organic matter [1–25% organic carbon by weight in weathered and unweathered shales (Petsch et al., 2000)] and represent a large reservoir of the Earth's reduced carbon and total nitrogen stocks (Berner, 1987; Houlton et al., 2018). Erosion and chemical weathering can mobilize shale-derived organic matter into other compartments, such as soils, alluvial sediments, rivers, lakes, and eventually oceans, through transport of suspended sediments. Evidence of mineral-bound

ancient organic carbon (OC) transport has been observed in modern river and marine systems (Blair et al., 2003; Goñi et al., 2005; Komada et al., 2004; Komada et al., 2005; Leithold et al., 2006; Raymond & Bauer, 2001a, 2001b). Transport of ancient OC may be greater in small mountainous rivers, where erosion rates are relatively high compared to larger and lower elevation rivers (Blair et al., 2003; Komada et al., 2004; Leithold et al., 2006). Galy et al. (2015) found that physical erosion rate exerts primary control over ancient (or petrogenic) OC transport to oceans, and estimated that ancient OC accounts for 22% of the global particulate organic carbon flux to oceans. Similarly, evidence of rock-derived N as a major source of N to soils and plants has recently been established and may be particularly important in montane systems where rock erosion rates are high (Houlton et al., 2018).

Organic matter in shale is derived from the remains of biological material of diverse origin that became incorporated into sediments during deposition and then underwent diagenesis (Petsch, 2017). Shale organic matter can be divided into two operationally defined pools, kerogen and bitumen, representing the insoluble and soluble fractions of organic matter, respectively, with kerogen making up >80% of shale organic matter (Petsch, 2017). Although shale kerogen is often considered to be refractory, evidence of dissolution and oxidation of shale-derived OC has been observed in shale weathering profiles (Leythaeuser, 1973; Petsch et al., 2000; Petsch et al., 2001) and in high dissolved organic carbon concentrations emanating from shales (Morrison et al., 2012; Schillawski & Petsch, 2008). Shale-derived OC contains no radiocarbon (^{14}C) due to radioactive decay over millions of years; thus, radiocarbon measurements can be used to distinguish between OC recently fixed from the atmosphere and ancient shale-derived OC. Incorporation of ^{14}C depleted OC into biomass has been observed both in zooplankton in the Hudson River (Caraco et al., 2010) and microbes isolated from black shale (Petsch et al., 2001), providing evidence that kerogen may be susceptible to biological assimilation and mineralization.

In mountainous watersheds, rivers transport both mineral and organic matter from steeper terrain and deposit it into floodplains where river water moves more slowly, meandering across broad unconfined valleys (Sutfin et al., 2016; Wohl et al., 2012). The floodplains of meandering rivers are biologically and hydrologically dynamic zones that are built upon alluvium and may serve as a large sink for carbon (Sutfin et al., 2016; Wohl et al., 2012). There are three primary sources of organic matter in floodplain sediments: (1) river-deposited organic detritus (e.g., plant debris), (2) litter input from riparian-zone vegetation, and (3) mineral-associated organic matter deposited by the river (i.e., from erosion of upland soils and rocks). In a shale-dominated landscape, alluvium containing shale kerogen and kerogen-containing shale bedrock (underlying alluvium) may be additional sources of OC. While little is known about the relative abundance of shale-derived OC in floodplain sediments, Blattmann et al. (2019) estimated that 30% of the OC buried and sequestered in a perialpine lake is derived from petrogenic OC. Estimates of global ancient OC storage in terrestrial freshwater basins range from 18 to 27 Tg OC/year (Blattmann et al., 2019; Meybeck, 1993). Shale-derived kerogen and vegetation-derived organic matter each have distinct initial chemical characteristics and potentially different reactivity, which may affect their ultimate fate in the river system with respect to storage, mineralization, and degradation. In large river basins with extensive floodplains (e.g., Ganges-Brahmaputra and Amazon) 30–50% of the ancient OC may be mineralized during transport to oceans (Bouchez et al., 2010; Galy et al., 2008), while river systems with rapid transport times show minimal mineralization of ancient OC (Blair et al., 2003; Kao et al., 2014).

In this study, we focus on sediments located in a floodplain of the East River, a mountainous watershed located in the Rocky Mountains near Gothic, CO, USA. Cretaceous Mancos Shale is the predominant form of bedrock across the East River watershed (Gaskill et al., 1991). The goals of this study were to (1) determine the relative abundance of shale-derived and plant-derived OC in floodplain sediments and (2) provide information on the relative chemistry and mobility of these two sources of OC within floodplain sediments. Sediment cores were collected along transects across an active and cutoff meander in the floodplain of a meandering section of the East River. The sampling locations represent a range of floodplain environments with differing degrees of deposition, erosion, and soil development. The sediments were subjected to density separations in order to separate the plant litter-derived OC from mineral-associated OC. Chemical extractions of sediments provided information on the mobility and chemical associations of the OC. Radiocarbon measurements were used to determine the ^{14}C age of the OC and provide information on the relative abundance of modern plant-derived and ancient shale-derived OC. Samples were

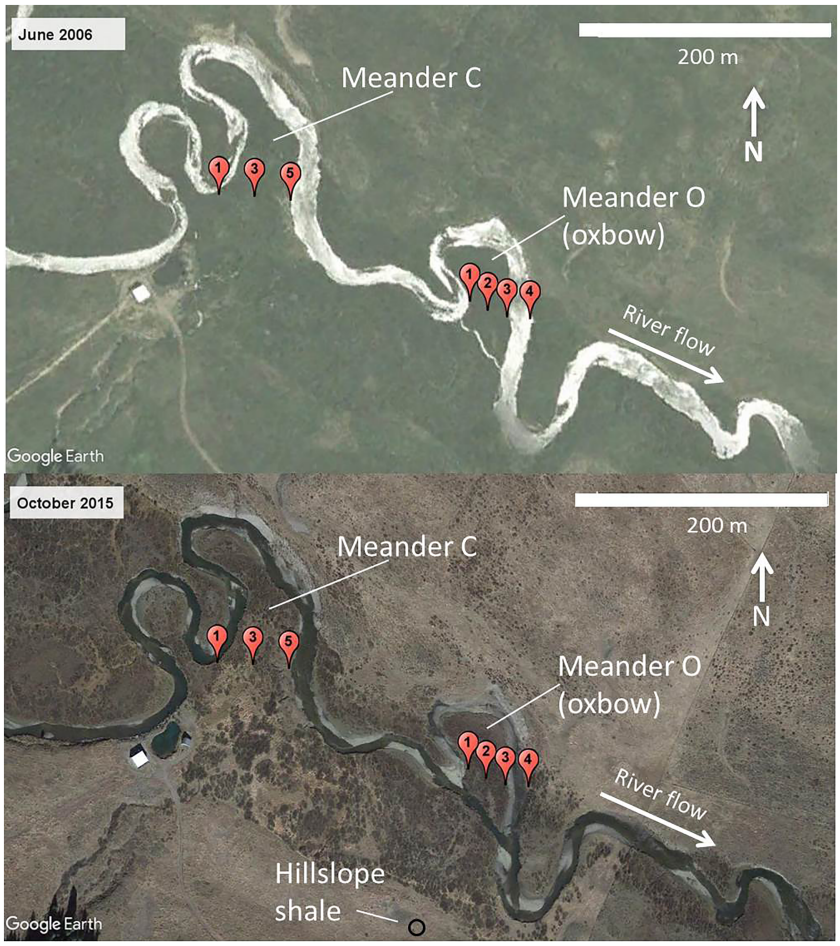

Figure 1. Aerial images of East River floodplain from (top) June 2006 before the oxbow was cut off and (bottom) October 2015 after the oxbow was cut off showing core locations. Sediment cores in Meander C were collected from the cut bank (MCP-1), middle (MCP-3), and point bar (MCP-5). Sediment cores in Meander O (oxbow) were collected from the cut bank (MOP-1), middle (MOP-2), point bar (MOP-3), and the wetland formed in the old river bed (MOP-4). The location of the hillslope shale core (PLM-6) is also indicated.

characterized using a variety of techniques, including C and N content, $\delta^{13}C$ values, Fourier transform infrared spectroscopy (FTIR), and C spectroscopy (scanning transmission X-ray microscopy [STXM] and near-edge X-ray absorption fine structure spectroscopy [NEXAFS]) to provide information on the chemistry of the various pools of OC.

2. Materials and Methods

2.1. Field Site Description and Sediment Sampling

The field site is located in a high-elevation, mountainous watershed of the East River located near Gothic, CO, USA. This watershed is the location of the Watershed Function Scientific Focus Area (SFA) led by Lawrence Berkeley National Laboratory (Hubbard et al., 2018). Sediment samples were collected from the floodplain of a meandering reach of the East River (Lower Montane Floodplain site) at an elevation of 2,760 m. The floodplain valley is approximately 200 m wide in this location, with the river meandering across nearly the entire valley (Falco et al., 2019; Wainwright & Williams, 2017). Sediments were collected along transects across an active (Meander C) and cutoff (Meander O/oxbow) meander (Figure 1) in September 2016 and July 2016, respectively. Cores were collected from the cut bank (upstream location; MOP-1, MCP-1), middle (MOP-2, MCP-3), and point bar (downstream location; MOP-3, MCP-5) in both meanders and a wetland section of the oxbow located in the former river channel (MOP-4). The official SFA project designations (numbers) are included here to allow the reader to reference other data and information

from these locations that may be available currently (e.g., Dwivedi et al., 2018) or in the future; the reader is referred to the SFA website (watershed.lbl.gov) for current data availability and publications. GPS coordinates for all sampling sites can be found in Table S1 in the supporting information. The oxbow was cut off between 2006 and 2011 when water broke through the neck of the meander (dated from historical aerial imagery; Figure 1). The oxbow becomes filled with water and is hydrologically connected to the main river channel during periods of peak discharge during the spring snowmelt (May–July). During periods of low discharge (approximately August–April), the oxbow channel drains leaving isolated patches of standing water. The wetland location is located in one of these permanently wet sections in the former river channel and is vegetated with marsh plants. Portions of both the active meander (Meander C) and the oxbow (Meander O) floodplains may become saturated annually during periods of peak discharge when the river overflows its banks. Vegetation is dominated by *mountain willow* in both Meander O and Meander C, with some *American dwarf birch, Potentilla*, and grasses (Falco et al., 2019). In both locations, sediment profiles consist of a layer of fine-grained material (<2 mm) ranging from 20 to 90 cm deep overlaying coarse-grained alluvium (sand, gravel, and cobbles). Alluvial materials are underlain by weathered shale at depth of approximately 1–2 m. The riverbed in the reach of the river being studied consists of a relatively thin (<1 m) layer of coarse alluvium underlain by weathered shale.

Sediment samples were collected in approximately 15-cm increments using a 5-cm-diameter soil core sampler (with slide hammer) until coarse alluvium was reached. After reaching coarse alluvium, sediment was sampled using an 8.3-cm-diameter bucket auger. Sediment samples were placed in polyethylene bags, sealed into aluminized biaxially oriented polyethylene terephthalate (Mylar™) bags containing O_2 absorbers (IMPAK™ Corporation), shipped to the laboratory, and stored at 4 °C until processing in order to preserve anaerobic conditions observed in some cores. Sediment samples were then sieved through a 2-mm sieve under field-moist conditions in a Coy anaerobic chamber filled with a gas mixture of 97% N_2 and 3% H_2. All analyses were performed on the <2-mm sediment fraction. Note that STXM analyses were performed on separate cores collected nearby representing the cut bank and middle of the meander.

Shale samples were collected from a hillslope location adjacent to the floodplain site (Figure 1; SFA name PLM-6) and from a shale outcrop on Gothic road (SFA name GRO). At the hillslope, a continuous vertical core to a depth of approximately 10 m below ground surface was collected using a track-mounted drill rig and a 0.14-m-diameter ODEX drilling bit. A shale weathering profile was observed from 1 to 3 m below ground surface. The sample denoted "Pristine" was subsampled from a piece of solid core at a depth of 9 m. Between 2 and 3 m below ground surface, numerous fractures were observed along with iron oxide discoloration. The sample denoted "Weathered" was subsampled at a depth of 2.7 m from within the weathering region of one such fracture surface. At the GRO site, a horizontal core 1 m above the ground surface and approximately 1 m long was collected from the outcrop using a hand drill with a 24.5-mm-diameter diamond drilling bit using water as a drilling fluid. The sample denoted "Top" was taken from the exposed section of the core, which exhibited signs of weathering such as iron oxide discoloration. The samples denoted "Middle" and "Bottom" were subsampled at depths of approximately 40 and 80 cm in the core.

A summary of the various processing and analytical techniques applied to the shale and sediment samples is shown in Figure S1 in the supporting information.

2.2. Density Fractionations

Sieved sediment samples were separated into three density fractions using the methods described by McFarlane et al. (2013), which was a modified version of the methods described by Golchin et al. (1994) and Swanston et al. (2005). This method yields three fractions, a free light fraction (FLF) representing unprotected OC, an occluded light fraction (OLF) representing OC physically protected inside aggregates, and a heavy fraction (HF) representing OC closely associated with sediment minerals, including shale kerogen.

Sediments were separated by density using low C and N sodium polytungstate (SPT-0, Geoliquids, Inc.) adjusted to a density of 1.65 g/mL. Of the SPT, 80 mL was added to 20 g of air-dried sediment, the bottle was gently inverted to wet all sediment, and samples were allowed to sit for 1 hr. Samples were then centrifuged at 4,710×*g* for 1 hr in a swinging bucket rotor. The floating material (FLF) was aspirated and rinsed thoroughly with MilliQ water to remove residual SPT. Sediment remaining at the bottom of the bottle was

mixed in SPT for 1 min at 1,700 rpm using a benchtop mixer (G3U05R, Lightnin, New York, NY) and sonicated in an ice bath for a total input of 100 J/mL (Branson 450 Sonifier, Danbury, CT) to disrupt aggregates. The sonifier output energy was calibrated according to Schmidt et al. (1999). The sample was allowed to sit for 1 hr, then centrifuged as above, and allowed to sit overnight. The floating material (OLF) was then aspirated and rinsed thoroughly as above. The remaining sediment is the HF, and was repeatedly rinsed with 150 mL of 0.15 M $CaCl_2$ and 0.01 M HCl. This dilute solution was used in place of MilliQ water to ensure sedimentation of clay particles during washing and centrifugation. After rinsing, all samples were transferred to preweighed aluminum tins and dried at 55 °C until all standing water had evaporated, then dried at 105 °C for 48 hr. Samples were weighed and ground either in a ball mill with tungsten-carbide balls (FLF and HF) or by hand in an agate mortar and pestle (OLF).

2.3. Sediment Extractions and OC Isolation

Sediment samples were extracted in order to provide information on the mobility and associations of sediment-associated OC. A sequential extraction using 0.01 M NaCl followed by 0.1 M sodium pyrophosphate (PP) was used to extract the water-soluble and metal-complexed OC, respectively, based on the method of Fox et al. (2017). A separate extraction using 0.5 M HCl was used to extract acid-soluble OC. Sediment-free method blanks were run and analyzed for dissolved OC for each extraction in the same manner as samples in order to check for contamination; dissolved OC in blanks was below the detection limit (0.2 mg/L) for all extractions and no solid was observed for blank extractions which were freeze-dried.

The sequential NaCl-PP extractions were performed as described by Fox et al. (2017), except that 0.01 M NaCl was used in place of the MilliQ water to more closely mimic the pore water ionic strength found in the field. Approximately 30 g of field-wet sediment was weighed into a 300-mL polycarbonate bottle and 150 mL of 0.01 M NaCl was added and allowed to mix for 20 hr. Samples were then centrifuged (25,000×*g* for 30 min) and the solution was filtered through a 0.22-μm filter (Acrodisc Supor). The remaining sediment was then extracted with 150 mL 0.1 M sodium pyrophosphate (pH 10) for 20 hr, then centrifuged, and filtered in the same manner as the NaCl extraction. A portion of the NaCl and PP extracts was retained for ICPMS and dissolved organic carbon analysis. NaCl extracts were acidified to pH 2 with 1 M HCl, bubbled with ultrahigh-purity N_2 gas to remove all inorganic carbon, and freeze dried. PP extracts were acidified to pH 2 with 6 M HCl and were allowed to sit overnight to ensure that OC precipitation was complete, then centrifuged at 20,000×*g* for 30 min. The supernatant (containing acid-soluble OC) was carefully removed to a clean bottle. The precipitated OC was transferred to pre-rinsed 1-kDa dialysis tubing (Spectra-Por 7) using approximately 7 mL of 0.012 M HCl (pH 2) and dialyzed against 0.012 M HCl for approximately one week in 1-L glass bottles, changing dialysis solution daily, then freeze-dried. This represents the PP >1-kDa fraction. PP samples containing acid-soluble OC were pumped through a preconditioned solid-phase extraction (SPE) column (Agilent Bond-Elut PPL, 200 mg) using a peristaltic pump with Tygon MHLL pump tubing and eluted with 5 mL methanol into a glass vial according to Dittmar et al. (2008). Samples were then placed in a vacuum desiccator to remove all methanol, redissolved in 5-mL MilliQ water, and freeze-dried. This represents the PP-SPE fraction.

For HCl extractions, approximately 3 g of field-wet sediment was weighed into a 50-mL polypropylene centrifuge tube and 15 mL of 0.5 M HCl was added in a Coy anaerobic glove bag (97% N_2, 3% H_2). Samples were mixed on an end-over-end sample rotator for 20 hr, then centrifuged (10 min at 7,000×*g*), and filtered through a 0.22-μm PVDF filter. Extractions were performed in duplicate and the average and standard deviation of the replicate extracts is reported. OC was isolated from selected HCl samples using SPE columns in the same manner as PP-SPE samples.

Total free iron oxide content was determined on the sediment using the citrate-bicarbonate-dithionite method (CBD). Air-dried sediment samples were ground to <125 μm in a ball mill using tungsten-carbide balls and then extracted with 0.3 M sodium citrate, 0.1 M sodium bicarbonate, and sodium dithionite (added in two 0.5-g portions) at 80 °C on duplicate samples (Loeppert & Inskeep, 1996). The extracts were then filtered through a 0.45-μm PVDF syringe filter and analyzed for Fe. Extractions were performed in duplicate and the average and standard deviation of the replicate extracts is reported.

2.4. Analytical Procedures

2.4.1. Extracted Organic Carbon and Metals

Organic carbon concentrations were determined in extract solutions by nonpurgeable organic carbon on a Shimadzu TOC-V analyzer. Samples were acidified with HCl and purged with N_2 in order to remove inorganic carbon prior to analysis. Metal concentrations in extract solutions were measured by ICP-MS (Perkin-Elmer Elan DRC II). Samples were diluted with ultrapure 0.16 M nitric acid and spiked with internal standards prior to ICP-MS analysis. All data are expressed in terms of air-dry sediment weight.

2.4.2. Solid Phase Organic Carbon and Nitrogen

OC, total nitrogen (N), and $\delta^{13}C$ were measured on sediment samples and sediment density fractions (FLF, OLF, and HF). Organic fractions (FLF and OLF) were measured directly without any pretreatment. Sediment samples (bulk and HF) were air-dried and crushed to a fine powder in a ball mill using tungsten-carbide balls. Approximately 1 g of dried and ground sediment was treated with ~2 mL of 0.6 M HCl for 8 hr to remove inorganic carbon. The sediment was then washed twice with 40-mL MilliQ water and dried. After drying, the sediment was crushed and homogenized using a mortar and pestle prior to analyzing for OC, N, and $\delta^{13}C$. Either 30 mg (HF and bulk) or 1 mg (FLF and OLF) of dried sample was weighed and sealed in a Sn capsule. OC, N, and $\delta^{13}C$ for all samples were determined on an ECS 4010 Elemental Analyzer (Costech Analytical Technologies Inc., Valencia, USA) coupled to a Delta V^{plus} isotope ratio mass spectrometer (Thermo Fisher Scientific, Bremen, Germany). C/N ratios are calculated on a mass basis. Samples were analyzed in duplicate, and the average and standard deviation is reported.

Whole sediment samples (air-dried and milled) were also analyzed for total carbon and inorganic carbon (IC) on a Shimadzu TOC-V analyzer equipped with a solid sampling module by catalytically aided combustion oxidation at 900 °C (total carbon) and thermally aided oxidation at 200 °C after 20% phosphoric acid addition (IC). OC was determined by difference between total carbon and IC. Samples were analyzed in duplicate, and the average and standard deviation is reported.

2.4.3. Radiocarbon

Radiocarbon measurements were performed on ball-milled bulk sediments, sediment density fractions, and extracted OC (freeze-dried NaCl, PP-SPE, and PP >1 kDa). Bulk sediment and sediment HF were treated by acid fumigation with HCl vapors for 48 hr in a vacuum desiccator, then dried at 60 °C for 24 hr, and stored in a vacuum desiccator in order to remove inorganic carbon prior to radiocarbon analysis (Ramnarine et al., 2011). All samples were graphitized in the Houghton Carbon, Water and Soils Lab (USDA-FS Northern Research Station) according to Vogel et al. (1987) and radiocarbon measurements were conducted in 2018 at the DirectAMS facility in Bothell, WA, using an accelerator mass spectrometer (Zoppi et al., 2007). All results have been corrected for isotopic fractionation according to the conventions of Stuiver and Polach (1977), using $\delta^{13}C$ values measured on prepared graphite using the accelerator mass spectrometer. Two control samples were analyzed, including radiocarbon-free wood (Queets-A; Southon & Magana, 2010), which was used for background subtractions, and a modern-carbon standard (ANU sucrose; Srdoc et al., 1979). Both control samples were suspended in MilliQ water and freeze-dried in the laboratory, then graphitized, and analyzed for radiocarbon in the same manner as samples. No evidence of ancient-C contamination was observed in the modern-carbon standard. Radiocarbon abundances are presented in units of $\Delta^{14}C$, following the conventions of Stuiver and Polach (1977). The fraction of modern standard (FM) and conventional radiocarbon age are also calculated according to Stuiver and Polach (1977), with conventional radiocarbon age in radiocarbon years using the Libby half-life of 5,568 years. Error terms for radiocarbon measurements represent analytical error for the accelerator mass spectrometer measurement.

2.4.4. Carbon NEXAFS/STXM

To determine the relative abundance of specific C functional groups and degree of oxidation, shale samples were analyzed using C (1 s) NEXAFS at the Canadian Light Source in Saskatoon, Canada. Individual samples were gently ground by hand to break up large aggregates, slurried in deionized water, and pipetted onto In foils. After drying, C NEXAFS spectra were obtained using the spherical grating monochromator beamline 11ID-1 (Regier et al., 2007). Step scan mode (0.25-eV steps from 270 to 320 eV) was used to minimize X-ray damage. A dwell time of 20 ms was used between scans. Individual spectra were collected at new locations on each sample for a total of 40 to 60 scans. The beamline exit slit was set at 25 mm, and the fluorescence yield data were collected using a two-stage microchannel plate detector. The resulting spectra were averaged for each sample and the averaged spectrum was baseline-normalized to zero and subsequently

normalized to the beamline photon flux (I_o) from a separate Au reference foil. Each spectrum was calibrated to the carboxylic acid peak (288.5 eV) of a citric acid standard. Pre-edge (270–278 eV) and post-edge (310–320 eV) and an E_0 (290 eV) values were used to perform an edge-step normalization in Athena (Demeter version 0.9.25, 2006–2016; Ravel & Newville, 2005).

STXM analyses were conducted at beamline SM 10ID-1 of the Canadian Lights Source in Saskatoon, Canada. Sediment samples were suspended in MilliQ water (1:10 soil:solution mass ratio) and an aliquot of 1 μL was drop deposited on Si_3N_4 windows (Silson) and dried under vacuum. The sample chamber for STXM image collection was He-filled to minimize attenuation of the soft X-rays. The energy was calibrated at the C 1s edge using the 3p Rydberg peak of gaseous CO_2 at 292.74 and 294.96 eV (Ma et al., 1991). Image sequences (also called "stacks") across the C K-edge were collected from regions of interest containing representative collections of particles for all samples. Image stacks were recorded across the C K-edge (278–330 eV) with dwell times of 1 ms and a spatial resolution of 35–50 nm. Clean areas of the Si_3N_4 membrane were used to normalize the transmission signal obtained from analyzed regions of interest. Transmission images at energies below and at the relevant absorption edge energies were converted into optical density (OD) images [OD = ln(I0/I), with I0 being the incident photon flux and I the transmitted flux]. C NEXAFS spectra were extracted from the STXM stacks using Axis and then processed similarly to the bulk carbon spectra as described below.

Both bulk C NEXAFS spectra and the spectra extracted from the STXM data were processed in Athena. The pre-edge and post-edge contributions were subtracted using a linear function with coefficients chosen in order to minimize differences between the spectra in the energy range between 280 and 295 eV. The post-edge shape of the bulk shale spectra differed somewhat from the STXM spectra largely due to a large contribution from both carbonate and K peaks in the bulk spectra. Once normalized, all spectra were fit through the same process of spectral deconvolution in Athena. An arctangent function centered at 291 eV (width 0.5) was used to represent the edge step and two broad Gaussian functions centered at 292.5 and 300.7 eV (width 3) were used to represent the sigma bonding contributions to the spectra. The pi* transitions were represented by a series of eight Gaussian functions all with width 0.5 and energies shown in Table S2. During the fitting procedure the widths and positions of all functions were held constant and only the heights were allowed to vary. The sum of the total area of the eight peaks shown in Table S2 was used to normalize the contribution of each individual peak and normalized data are reported. The energy positions chosen were based on previous studies (Brandes et al., 2010; Cody et al., 1998; Francis & Hitchcock, 1992; Hitchcock et al., 1992) because of the importance of resonances in the aromatic and carbonate structures. The two resonances in Table S2 both listed as Functionalized Aromatic (carbonyl substituted) were maintained as separate peaks because of the visible contribution of resonances in that region in the spectra. Both spectral energies fall in the range of aromatic rings functionalized by different election withdrawing carbonyl structures, often referred to as aromatic ketone groups. A more detailed assessment of those two peaks was not attempted and they are grouped together in the discussion as functionalized aromatics.

2.4.5. FTIR and UV Spectroscopy

Soluble OC extracts were analyzed by UV-Vis absorption on a Thermo Scientific Aquamate Plus spectrophotometer over the 200–800-nm wavelength range in a 1-cm quartz cuvette, using a 1-nm step size. Specific UV absorbance ($SUVA_{254}$) values were calculated by dividing the absorbance at 254 nm (in m^{-1}) by the OC concentration (in mg/L). Freeze-dried sediment extracts and ball-milled density fractions of sediment were analyzed by ATR-FTIR (attenuated total reflection Fourier transform infrared spectroscopy) using a Thermo Scientific Nicolet iS50 FTIR equipped with a single-bounce diamond crystal. Samples were analyzed using a liquid-N_2 cooled MCT/A detector from 650 to 4,000 cm^{-1}, with 64 scans each. A background spectrum (air) was collected immediately prior to each sample. Atmospheric suppression, ATR correction, baseline correction, and intensity normalization were performed on background-corrected sample spectra using OMNIC software. Peak assignments are from Stevenson (1994) and Baes and Bloom (1989).

2.5. Statistical Analysis

One-way repeated measures analysis of variance was used to determine whether C/N ratios, $\delta^{13}C$ values, and $\Delta^{14}C$ values were significantly different across density fractions (FLF, OLF, HF, and bulk). When

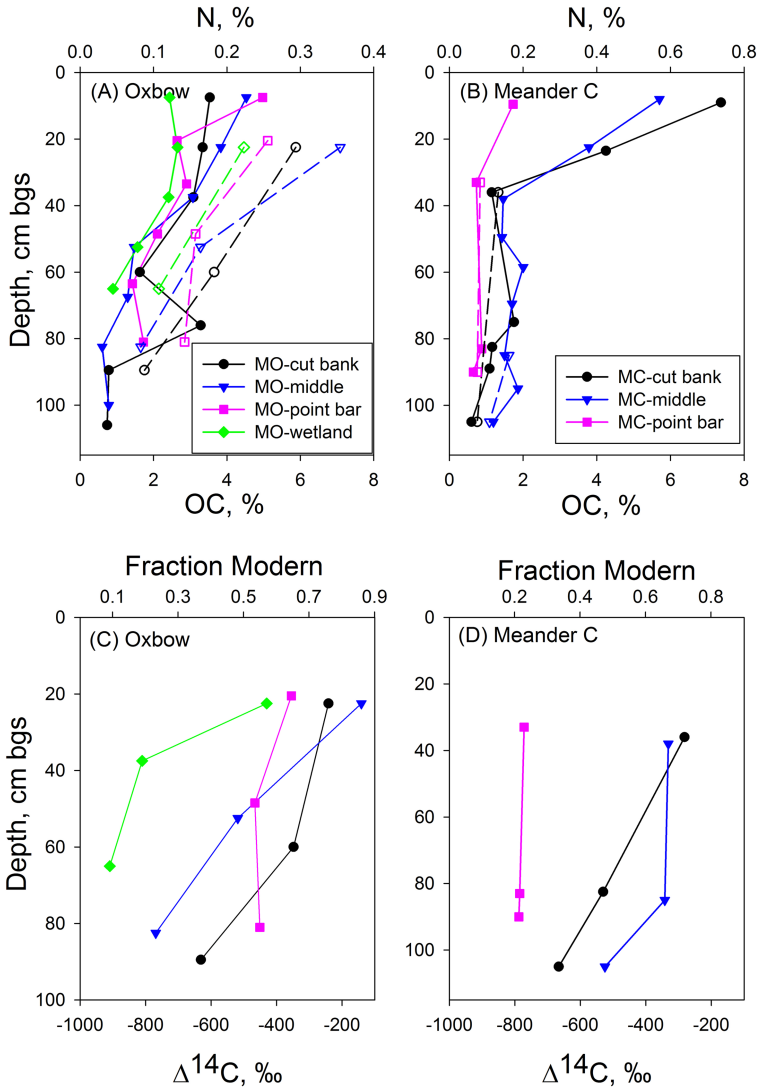

Figure 2. (a and b) Organic carbon (OC; solid lines and symbols) and nitrogen (N; dashed lines). (c and d) $\Delta^{14}C$ values, for oxbow and Meander C sediments as a function of depth. The $\Delta^{14}C$ and fraction modern values are shown for ^{14}C measurements. Oxbow location symbols and colors are the same for (a) and (c) and Meander C locations are the same for (b) and (d).

significant difference ($p < 0.05$) was observed, pairwise comparison across density fractions was performed using the Holm-Sidak method. Correlation was determined using the Pearson Product Moment correlation method using a p value of 0.05. All statistical analyses were performed using SigmaPlot software (Systat, Inc.).

3. Results

3.1. Organic Carbon, Nitrogen, and ^{14}C

Concentrations of OC, N, and $\Delta^{14}C$ for whole sediments are shown in Figure 2. OC and N concentrations are highly correlated for all samples ($R = 0.79$, $p < 0.001$), suggesting that most N is organic. The C/N mass ratio ranges from 7.3 to 13.4, with an average and standard deviation of 9.8 ± 1.7 for all samples. $\Delta^{14}C$ values range from −909 to −141‰ and generally decrease with depth, except for the two point bar locations, which are uniform with depth. Shale-derived OC is essentially ^{14}C-free ($\Delta^{14}C$ of approximately −1000‰) due to radioactive decay over millions of years; thus, $\Delta^{14}C$ values less than −800‰ indicate a large proportion of shale-derived OC. The point bar locations are less vegetated and have less fine-grained material (Figure 3)

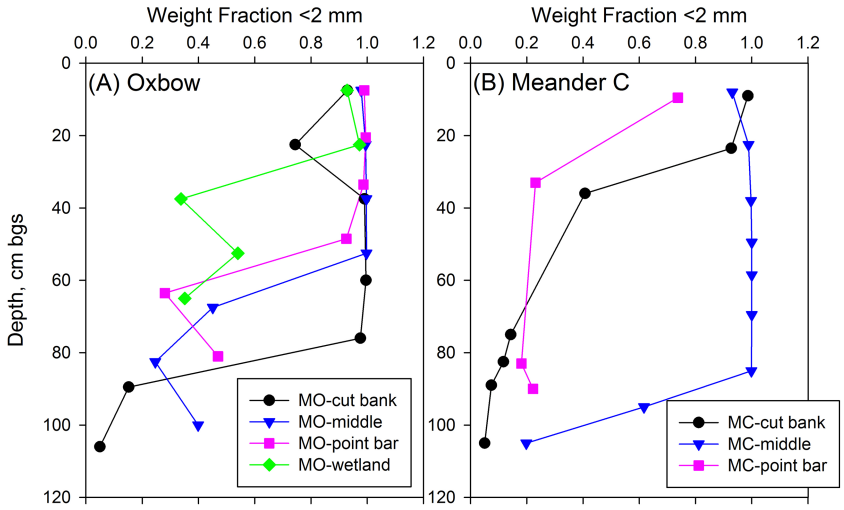

Figure 3. Sediment texture expressed in terms of weight fraction <2 mm as a function of depth for (a) Meander O (Oxbow) and (b) Meander C.

compared to the cut bank or middle of the meanders due to more recent deposition of sediments. The sediments in the oxbow wetland location (MO-wetland) also have highly depleted $\Delta^{14}C$ values below 30 cm. This wetland is located in the former river bed and contains a relatively thin layer of fine-grained sediment (0–30 cm) deposited on top of coarse alluvium. Concentrations of inorganic carbon range from 0 to 1.3% in bulk sediment (Figure S2), with higher IC concentrations generally present in the point bar (MO and MC) and MO-wetland locations.

3.2. Density Fractionations: OC, N, and Isotopes

Selected sediment samples were subjected to density fractionation in order to determine the amounts of OC, N, and ^{14}C present in mineral associated (HF) and light OC (FLF, OLF) fractions. The light fractions represent organic fractions of the sediment composed primarily of plant litter, where the OLF is occluded within aggregates, while the FLF is "free." The mineral fraction (or heavy fraction, HF) contains OC adsorbed to, or otherwise intricately associated with, mineral particles. Samples from the middle positions of Meander C and the Oxbow were chosen for this analysis in order to provide a contrast with depth for the two locations along with three additional samples from nearer the sediment surface. These samples cover a wide range in observed bulk sediment OC and $\Delta^{14}C$ (0.7–4.2% OC and −742 to −141‰ $\Delta^{14}C$). Concentrations of OC, N, and C isotopic values are shown for each density fraction in Table 1. Total mass recovery in density fractionations was 98–101%. Total recoveries of OC in density fractions ranged from 82 to 97%, except for the deepest MC-middle sample (100–110 cm), for which 67% of the OC was recovered. Recoveries of N in density fractionations ranged from 82 to 104%.

The largest amount of OC and N was recovered in the HF (average across all samples of 84 ± 6% OC and 95 ± 3% N), followed by OLF (11.5 ± 5.2% OC and 4.2 ± 3.1% N) and FLF (4.8 ± 2.3% OC and 1.3 ± 0.7% N), as shown in Figure 4. The fraction of OC found in the light fractions decreased with depth for MO-middle, while OC in the heavy (mineral-associated) fraction increased with depth. The same is true for N, although the effect is less pronounced due to a larger fraction of the N present in the HF compared to OC. However, no depth trends in the distribution of OC and N among fractions were observed for MC-middle.

OC concentrations averaged 33.2 ± 3.3, 35.2 ± 3.6, and 1.06 ± 0.14% across all samples for the FLF, OLF, and HF, respectively, while N concentrations averaged 0.99 ± 0.09, 1.39 ± 0.23, and 0.14 ± 0.06% for the FLF, OLF, and HF, respectively. The resulting C/N ratios show a decrease from FLF (33.5 ± 3.6) to OLF (26.0 ± 5.1) to HF (7.3 ± 0.8). The C/N ratios of the fractions are significantly different from one another ($p < 0.001$) and significantly different from the bulk C/N (9.2 ± 1.2), with the exception of the HF and bulk, which are not significantly different (Table 2). The $\delta^{13}C$ values varied

Table 1
Organic Carbon and Nitrogen Concentrations and $\delta^{13}C$ and $\Delta^{14}C$ Values in Bulk Sediment and Density Fractions of Sediment

Location	Depth (cm)	Fraction	OC (%)	N (%)	C/N	$\delta^{13}C$ (‰)	$\Delta^{14}C$ (‰)
MC-cut bank	29–43	bulk	1.15 ± 0.00	0.13 ± 0.00	8.7 ± 0.1	−25.8 ± 0.1	−281.7 ± 1.0
		FLF	35.71 ± 0.11	1.03 ± 0.01	34.5 ± 0.3	−27.1 ± 0.1	7.9 ± 2.7
		OLF	36.68 ± 0.05	1.81 ± 0.02	20.3 ± 0.2	−26.7 ± 0.1	4.5 ± 3.0
		HF	0.77 ± 0.05	0.11 ± 0.01	6.8 ± 0.6	−25.9 ± 0.1	−596.2 ± 1.0
MC-middle	29–47	bulk	1.46 ± 0.01	NA	NA	NA	−331.3 ± 1.0
		FLF	30.26 ± 0.02	1.03 ± 0.01	29.4 ± 0.2	−26.5 ± 0.0	184.0 ± 2.9
		OLF	37.32 ± 0.07	1.42 ± 0.00	26.4 ± 0.1	−25.5 ± 0.0	−76.8 ± 2.4
		HF	1.11 ± 0.05	0.15 ± 0.00	7.5 ± 0.4	−25.4 ± 0.0	−383.1 ± 1.2
MC-middle	80–90	bulk	1.50 ± 0.04	0.16 ± 0.00	9.2 ± 0.2	−25.6 ± 0.0	−341.9 ± 2.2
		FLF	29.02 ± 0.20	0.95 ± 0.00	30.6 ± 0.2	−26.6 ± 0.1	61.0 ± 3.4
		OLF	33.02 ± 0.24	1.38 ± 0.01	24.0 ± 0.2	−25.7 ± 0.1	−100.3 ± 3.8
		HF	1.18 ± 0.03	0.16 ± 0.00	7.5 ± 0.3	−25.5 ± 0.1	−399.0 ± 2.0
MC-middle	100–110	bulk	1.20 ± 0.06	0.11 ± 0.00	11.0 ± 0.7	−25.7 ± 0.0	−524.8 ± 1.3
		FLF	34.22 ± 0.27	1.13 ± 0.01	30.3 ± 0.4	−26.4 ± 0.0	−44.6 ± 2.7
		OLF	36.54 ± 0.21	1.44 ± 0.02	25.4 ± 0.3	−25.5 ± 0.1	−159.2 ± 2.0
		HF	0.69 ± 0.01	0.09 ± 0.00	7.4 ± 0.3	−25.9 ± 0.0	−628.4 ± 1.4
MC-point bar	19–47	bulk	0.73 ± 0.01	0.08 ± 0.00	8.7 ± 0.1	−25.8 ± 0.0	−771.8 ± 1.5
		FLF	31.79 ± 0.27	0.84 ± 0.02	37.8 ± 0.9	−26.0 ± 0.0	11.0 ± 1.6
		OLF	28.66 ± 0.31	1.03 ± 0.01	27.7 ± 0.4	−25.3 ± 0.1	−177.9 ± 2.6
		HF	0.56 ± 0.03	0.08 ± 0.00	6.7 ± 0.3	−25.9 ± 0.0	−765.8 ± 0.8
MO-cut bank	50–70	bulk	1.63 ± 0.03	0.18 ± 0.00	8.9 ± 0.2	−25.3 ± 0.1	−348.0 ± 2.2
		FLF	36.34 ± 0.03	1.10 ± 0.01	33.2 ± 0.2	−26.6 ± 0.1	NA
		OLF	35.88 ± 2.09	1.45 ± 0.04	24.7 ± 1.6	−25.7 ± 0.1	NA
		HF	1.25 ± 0.01	0.17 ± 0.00	7.3 ± 0.1	−25.0 ± 0.2	NA
MO-middle	15–30	bulk	3.83 ± 0.06	0.35 ± 0.00	10.8 ± 0.2	−25.5 ± 0.1	−141.0 ± 2.8
		FLF	31.69 ± 0.15	0.95 ± 0.01	33.5 ± 0.4	−26.8 ± 0.0	96.0 ± 3.2
		OLF	31.56 ± 0.48	1.52 ± 0.00	20.7 ± 0.3	−25.7 ± 0.0	28.2 ± 3.1
		HF	2.41 ± 0.05	0.26 ± 0.00	9.1 ± 0.2	−25.6 ± 0.0	−228.1 ± 2.4
MO-middle	45–60	bulk	1.47 ± 0.01	0.16 ± 0.00	9.0 ± 0.1	−25.2 ± 0.1	−518.3 ± 1.7
		FLF	30.63 ± 0.39	0.94 ± 0.00	32.5 ± 0.4	−25.7 ± 0.0	−32.4 ± 3.5
		OLF	36.29 ± 0.37	1.35 ± 0.00	26.8 ± 0.3	−25.4 ± 0.0	−153.2 ± 2.8
		HF	1.07 ± 0.02	0.15 ± 0.00	7.2 ± 0.2	−25.2 ± 0.1	−224.3 ± 1.6
MO-middle	75–90	bulk	0.60 ± 0.00	0.08 ± 0.00	7.3 ± 0.0	−26.0 ± 0.0	−769.2 ± 1.5
		FLF	38.96 ± 0.07	0.97 ± 0.02	40.2 ± 0.9	−25.6 ± 0.1	NA
		OLF	40.87 ± 0.48	1.09 ± 0.01	37.6 ± 0.5	−25.0 ± 0.1	−348.6 ± 2.0
		HF	0.48 ± 0.01	0.08 ± 0.00	6.1 ± 0.2	−25.9 ± 0.0	−853.0 ± 0.5

NA = data not available.

over a narrow range across samples, with FLF being significantly lighter ($p < 0.001$) from all other fractions (−26.37 ± 0.50, −25.60 ± 0.48, and −25.58 ± 0.35 for FLF, OLF, and HF, respectively); no other significant differences were observed in $\delta^{13}C$ values.

The $\Delta^{14}C$ values also decrease from FLF to OLF to HF (Table 1 and Figure 5). The FLF values range from −44.6 to 184.0‰, corresponding to almost entirely modern carbon (fraction modern 0.96–1.10). The OLF $\Delta^{14}C$ values range from −348.6 to 28.2‰, corresponding to a fraction modern of 0.66 to 1.04, and the HF $\Delta^{14}C$ values range from −853 to −224‰, corresponding to a fraction modern of 0.15 to 0.78. In all cases except for MO-middle, 45–60 cm, the HF has a lower $\Delta^{14}C$ value (older) than for the bulk sediment. If we exclude the $\Delta^{14}C$ for this HF sample as an outlier, then the FLF-OLF and HF-bulk fraction pairs are significantly different from one another at the $p < 0.1$ level, and all other pairs are significantly different at the $p < 0.001$ level (Table 2). The $\Delta^{14}C$ values of all density fractions generally decrease with depth for both the MC-middle and MO-middle sediments (Figure 5).

Correlations between several variables of the sediment density fractions were performed in order to elucidate the controls on OC concentrations and ages in each fraction. These correlations are shown, along with the correlation coefficients and p values, in Figure 6. For the HF, the CBD-extractable Fe is positively correlated with the OC content, and HF $\Delta^{14}C$ values are positively correlated with both the C/N ratio and OC content of the HF. By contrast, the $\Delta^{14}C$ values of the OLF are negatively correlated with

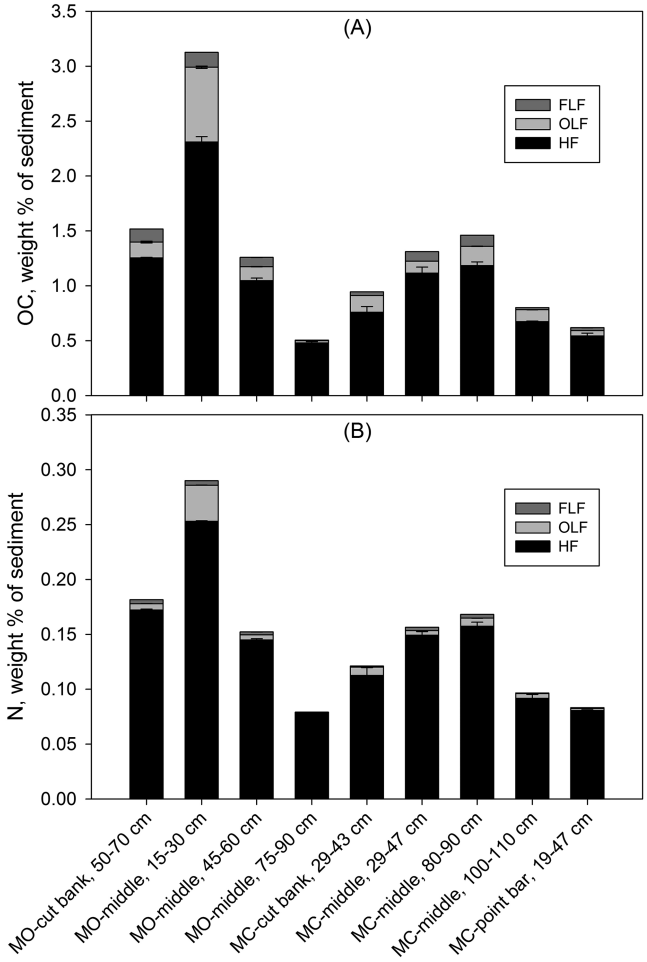

Figure 4. (a) Organic carbon and (b) nitrogen in sediment density fractionations expressed as weight % of dry sediment.

the C/N ratio of the OLF. $\Delta^{14}C$ values for density fractions are plotted against bulk sediment $\Delta^{14}C$ and OC in Figure 7. The OLF and HF $\Delta^{14}C$ values are positively correlated with both bulk $\Delta^{14}C$ and OC.

3.3. Extraction of Sediment-Associated OC

The total amount of OC recovered from extractions ("whole") are shown along with OC recovered in purified PP fractions (PP-SPE and PP >1 kDa) and $\Delta^{14}C$ values for selected samples in Table 3. Additional data for HCl extractions are presented in Figure S3. In general, extractable OC decreases with depth, following the trend of bulk sediment OC. Pyrophosphate extracted the most sediment OC (5.7–16.6% of total sediment OC), followed by HCl (1.5–6.0%), with NaCl extracting the least (0.13–0.74%). $\Delta^{14}C$ values range from −345 to −7.2‰ in the NaCl fraction, −145 to 0.1‰ in the PP-SPE fraction, and −557 to −115‰ in the PP >1-kDa fraction. The $\Delta^{14}C$ values of the PP >1−kDa fraction are similar to bulk sediment $\Delta^{14}C$ values, while the NaCl and PP-SPE $\Delta^{14}C$ values are similar to the OLF (Figure 7). All OC fractions from extractions and density fractionations, with the notable exception of FLF, have variably depleted $\Delta^{14}C$ values which are significantly correlated with bulk $\Delta^{14}C$ (Figure 7a). The PP >1-kDa fraction is also significantly correlated with bulk sediment OC (Figure 7b).

3.4. Chemical Characterization of Sediment OC

3.4.1. FTIR and UV Spectroscopy

Example FTIR spectra are shown in Figure 8 for extractable OC (HCl-SPE, PP-SPE, and PP >1 kDa) compared with solid-phase OC from density fractionations (FLF and OLF). All spectra are presented in Figures S4 and S5. There is a large difference in the predominance of the C–O–C stretching peak (from polysaccharides) around 1,000 cm^{-1} between the solid-phase and extracted OC fractions. The OLF and FLF also have much smaller COOH peaks (at 1,710 and 1,220 cm^{-1}) compared to extracted OC, with the 1,500–1,800-cm^{-1} region dominated by the C=C peak around 1,600 cm^{-1}. These results are consistent with the presence of primarily lignin and cellulose in FLF and OLF and more oxidized and processed material in the extractable fractions (HCl-SPE, PP-SPE, and PP >1 kDa). Differences between OLF and FLF are minor. However, some differences are observed between the different extractable OC fractions. Namely, the COOH (1,710 cm^{-1}) to C=C (1,600 cm^{-1}) peak ratios are different across fractions, with C=C peaks increasing from HCl-SPE to PP-SPE to PP >1-kDa fractions. The C–H stretching peaks (2,850, 2,925 cm^{-1}) are also higher in the PP >1-kDa fractions than the HCl-SPE and PP-SPE fractions, suggesting that the PP >1-kDa fraction is higher in more saturated/lipid-like compounds. Comparison of FTIR spectra for each fraction of OC across samples shows some small differences in the COOH to C=C ratio for extracted OC and in the C=C to C–O–C ratio for OLF and FLF samples (Figures S4 and S5). However, these differences are small, suggesting that the OC is chemically similar in each fraction. $SUVA_{254}$ values, which have been shown to be correlated with aromaticity (Weishaar et al., 2003), vary between 0.84 and 3.66 L/mg m for

Table 2
Results From ANOVA Analysis of Statistical Differences for C/N Ratios, $\delta^{13}C$, and $\Delta^{14}C$ Values Showing p Values for Pairs of Density Fractions and Bulk Sediment

	FLF-OLF	FLF-HF	FLF-bulk	OLF-HF	OLF-bulk	HF-bulk
C/N	<0.001	<0.001	<0.001	<0.001	<0.001	0.275
$\delta^{13}C$	<0.001	<0.001	<0.001	0.986	0.952	0.996
$\Delta^{14}C$[a]	0.051	<0.001	<0.001	<0.001	<0.001	0.063

[a]For $\Delta^{14}C$ statistical analyses, the outlier data point (HF, MO-middle, 45–60 cm) is excluded.

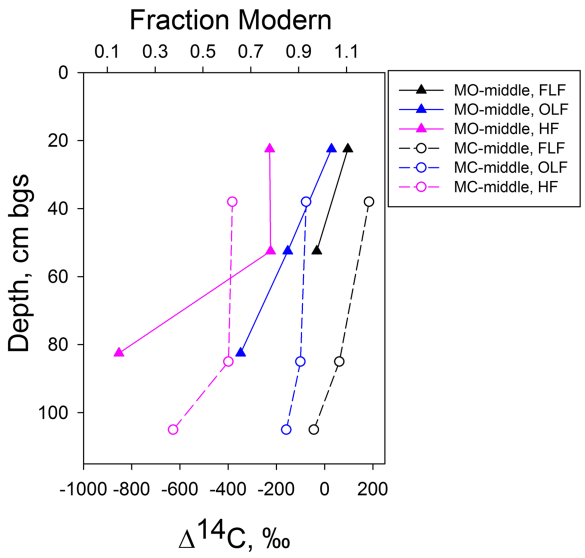

Figure 5. $\Delta^{14}C$ values and corresponding fraction modern for density fractions of sediments as a function of sediment depth. Samples are from the middle of Meander O and Meander C. Note that not enough FLF sample was recovered for MO-middle, 75–90 cm for $\Delta^{14}C$ analysis.

NaCl whole extracts and between 4.82 and 7.42 L/mg m for the PP-SPE fraction (Table 3), indicating that the PP-SPE is more aromatic. OC extracted from Colorado River alluvial aquifer sediment (Rifle, CO) showed a similar trend of increasing aromaticity from water-extractable to PP-SPE to PP >1 kDa (Fox et al., 2017).

3.4.2. STXM and NEXAFS Investigation of Sediment Carbon

Carbon spectra were collected from sediment samples using STXM and compared with C NEXAFS spectra of shale samples from local hillslopes. Example spectra are shown in Figure 9 and peak fitting results are shown in Table 4. All spectra and composite maps are shown in Figures S6 and S7. The shapes of the shale spectra are generally very similar to each other as can be seen by the small standard deviations on the average in Table 4. However, there is variation in the carbonate content across shale samples, with a small increase in carbonate concentration in the weathered hillslope sample compared to the pristine sample. Similarly, there is a change from top/middle to bottom of the GRO profile. The shale spectra all have significant contributions of quinone and aromatic functional groups with smaller contributions of functionalized aromatic, aromatic (C–OH)/aliphatic, carboxylic, and alkyl–OH. With the exception of particle 4 from MC-middle the floodplain particles are also similar to each other, although more variable than the pure shale samples. Similar to the shale materials the floodplain particles also have a very strong contribution of aromatic type resonances. The differences between the shale and floodplain spectra include lower quinone, alkylated aromatic, and carbonate content and higher functionalized aromatic and carboxylic content in the floodplain samples. In contrast, particle 4 is clearly of a different type of carbon that is dominated by carboxylic groups and is consistent with spectra of microbial derived carbon.

4. Discussion

4.1. Evidence for Shale-Derived OC in Mineral-Associated Fractions

The $\Delta^{14}C$ values observed in the bulk sediment (−909 to −141‰) and mineral associated fraction (HF, −853 to −224‰) are much lower than is typically observed in soils (e.g., Hicks Pries et al., 2017; McFarlane et al., 2013; Schmidt et al., 2011; Schrumpf et al., 2013), although comparible values are observed in deeper horizons of old (3 kyr to 3 Myr old) soils (Baisden et al., 2002). There are two primary mechanisms by which low $\Delta^{14}C$ values could be observed in HF in our study: (1) presence of shale-derived OC and (2) unusually long aging of plant or microbial-derived OC through chemical alteration and mineral protection. Rock-derived OC has been implicated in low $\Delta^{14}C$ values observed in areas where OC-rich (e.g., shale) bedrock is present, including in soils (Hemingway et al., 2018; Longbottom & Hockaday, 2019; van der Voort et al., 2019), lake sediments (Blattmann et al., 2019; Vonk et al., 2016), and riverine suspended particulate matter (Kao & Liu, 1996; Vonk et al., 2016). Gurwick et al. (2008) observed ^{14}C ages of 10,650–17,050 years B.P. for buried organic sediment horizons in alluvial systems, with ^{14}C ages of 4,730 years B.P. for organic matter fragments. However, in our system, soil ages on the order of 5–10,000 years are unlikely due to the relatively young depositional environment of the floodplain. The $\Delta^{14}C$ values observed in FLF samples can be used to constrain the depositional age of vegetation-derived OC. The lowest $\Delta^{14}C$ value was observed for sample MC-middle at 100–110 cm and corresponds to a ^{14}C age of 300 years B.P. Based on this observation, shale-derived OC must be responsible for the extremely low $\Delta^{14}C$ values observed in these sediments. However, it should be noted that the wide range of $\Delta^{14}C$ values observed in the HF samples indicates that this fraction is not entirely composed of shale-derived OC, but is a mixture of shale-derived and relatively modern (<300 years old) vegetation-derived OC. The fraction modern ranges from 0.15 to 0.78 in the HF, indicating that varying amounts of relatively modern OC are tightly bound to the mineral fraction of the sediments.

Most of the OC (74–95%) and N (87–99%) is closely associated with the mineral fraction of the sediment (HF). Similarly, Graf-Rosenfellner et al. (2016) found that most of the OC was associated with the HF

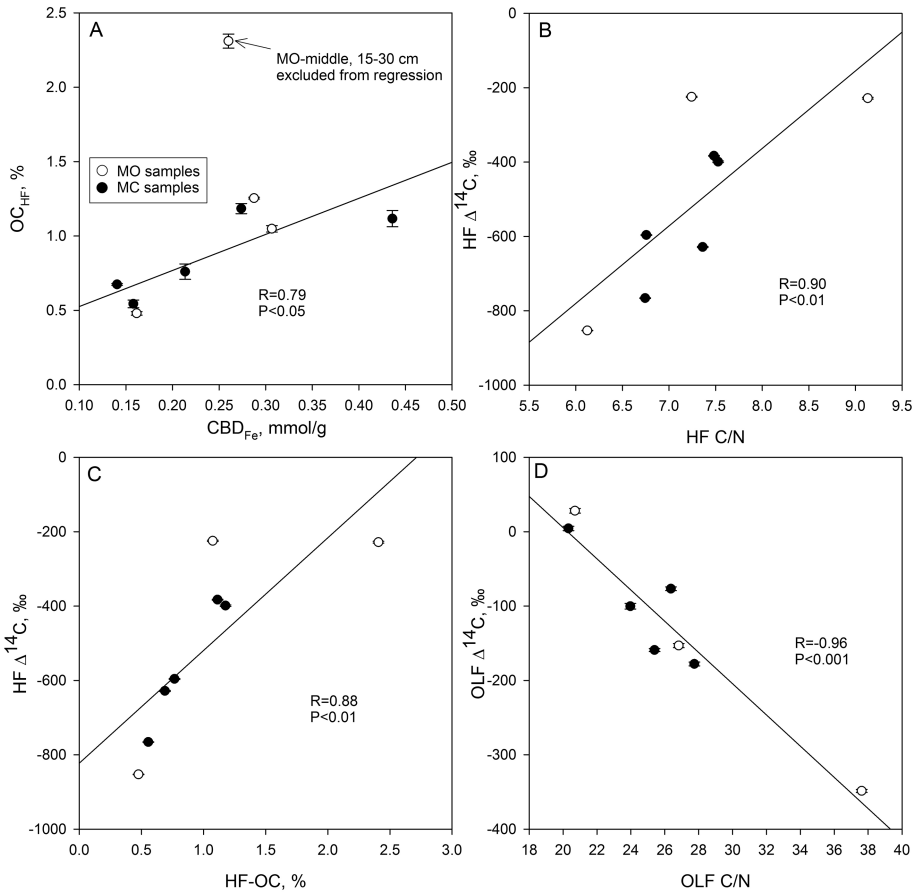

Figure 6. Correlations between variables (a) CBD-extractable Fe and OC coming from HF (expressed as weight % of dry sediment), (b) C/N ratio and $\Delta^{14}C$ value of HF, (c) HF OC concentration (weight % of HF) and $\Delta^{14}C$ value of the HF, and (d) C/N ratio and $\Delta^{14}C$ value of OLF. The correlation coefficient (R) is shown along with the p value in each plot. Note that the MO-middle, 15–30 cm sample was excluded from the regression in (a) due to the large OC content.

(50–97%) for sediments and floodplain soils of the Danube River. In a study of Sacramento-San Joaquin Delta river bed sediments, Wakeham and Canuel (2016) found that the majority of OC was present in mesodensity fractions (1.6–2.5 g cm^{-3}); however, this fraction contains a large number of mineral-organic aggregates which were not dispersed in their density fractionation protocol and thus direct comparison is difficult. Correlations between HF $\Delta^{14}C$ values and C/N and HF OC concentrations (Figures 6b and 6c) provide further evidence that HF-OC is derived from a mixture of ancient shale OC and modern OC. HF samples with the lowest $\Delta^{14}C$ values (<−700‰), which are primarily made up of shale-derived OC, are characterized by low C/N ratios (6–7) and OC concentrations around 0.5%. By contrast, the HF sample with the highest $\Delta^{14}C$ value, which is composed of primarily modern OC, is characterized by higher C/N ratio (9.1) and higher OC concentration (2.4%).

The OC content in the HF is significantly correlated with CBD-extractable Fe (if the MO-middle 15–30-cm data point which has much higher OC content is excluded) as shown in Figure 6a. CBD-extractable Fe is a measure of the total Fe oxide content of the sediment. Through examination of the data in Figures 6a and 6c, we can estimate that the shale contributes a background OC content of 0.5% and CBD-extractable Fe of 0.15 mmol/g. HF samples with a higher contribution from modern C also have higher CBD-extractable Fe contents. An increase in iron oxide content commonly occurs as pyrite is oxidized during shale weathering and soil formation (Chigira & Oyama, 2000; Evangelou & Zhang, 1995; Littke et al., 1991; Strawn et al., 2002). This suggests that iron oxide formation may increase the OC content of the HF through adsorption or occlusion of more modern OC. Other studies have also shown evidence of the important role of Fe oxides in

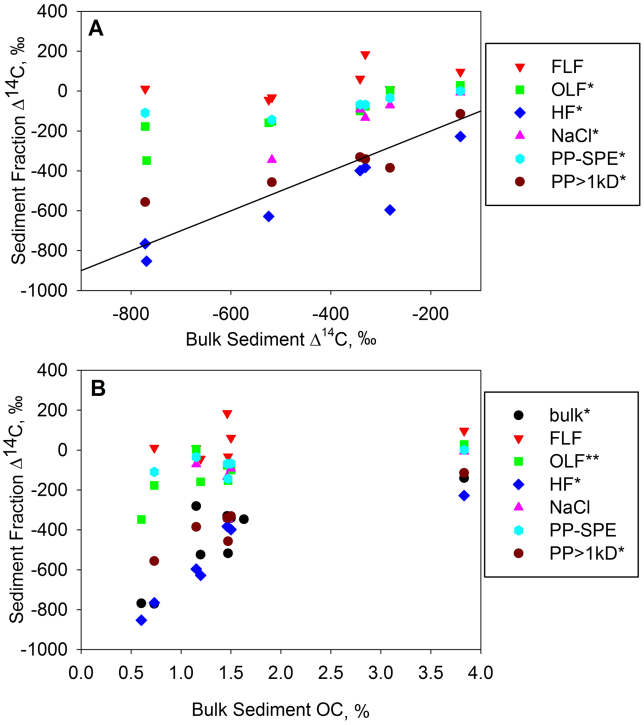

Figure 7. $\Delta^{14}C$ data for density separations (FLF, OLF, HF) and extractions (NaCl, PP-SPE, PP >1 kDa) plotted against (a) bulk sediment $\Delta^{14}C$ and (b) bulk sediment OC. In the legends, * and ** indicate OC fractions which are significantly correlated with bulk sediment $\Delta^{14}C$ or OC at the $p < 0.05$ and $p < 0.1$ levels, respectively. The line in (a) is the 1:1 line such that values above the line are higher than bulk $\Delta^{14}C$ and values below the line are lower than bulk $\Delta^{14}C$.

sequestering OC in soils and marine sediments through a combination of adsorption, co-precipitation, and complexation (Lalonde et al., 2012; Wagai et al., 2011; Wagai & Mayer, 2007).

4.2. Estimated Contribution of Shale-Derived OC in Floodplain Sediments

The fraction of modern C (based on $\Delta^{14}C$ measurements) for bulk sediment (<2 mm) ranges from 0.09 to 0.87. A weighted average which takes the TOC content and relative mass of sediment <2 mm into account can be calculated to determine the fraction of modern C present in the whole sediment-carbon pool according to the following equation:

$$FM_T = \frac{\sum FM_i OC_i M_i}{\sum OC_i M_i + \sum OC_g(1-M_i)} \quad (1)$$

where FM_T is the total fraction modern, FM_i is the fraction modern for the individual samples, OC_i is the organic carbon concentrations of the individual samples, M_i is the sediment weight fraction less than 2 mm, and OC_g is the organic carbon concentration of the >2-mm fraction of sediment. OC_g was not measured directly; therefore, we estimate that it has a value between 0.0 and 0.5%, representing granitic (carbon-free) and shale end-members, and has a FM of 0. This calculation results in a weighted average for fraction modern OC of 0.53–0.63 across all samples, with a slightly higher value of 0.68–0.72 for shallow sediments (15–45 cm) and lower value of 0.37–0.51 for deeper sediments (41–110 cm). If we assume that the fresh plant-litter derived OC has a FM of 1.0, the percentage of shale-derived carbon ($\%C_{shale}$) can then be estimated using a simplified two-pool mixing model as shown in equation (2):

$$\%C_{shale} = 100\times(1-FM_T) \quad (2)$$

Based on equation (2) and the available ^{14}C data, we can estimate that 37–47% of the OC in the 15- to 110-cm depth of the floodplain is derived from shale. However, while TOC concentrations were measured for the entire sediment profile, ^{14}C measurements were limited to three 15-cm core sections for each location. In order to extrapolate this estimate to represent the entire floodplain pool of OC, we have calculated the contribution of shale OC using the following assumptions: (1) the FM of the top 15 cm ranges from 0.87 to 1.00 and (2) the FM of intermediate and deeper sediment layers can be interpolated by averaging the FM of the layers above and below. Based on these assumptions, we estimate that 23–34% of the entire floodplain OC pool is derived from shale (see details in Table S3). Taking either of these estimation approaches, it is clear that shale-derived carbon contributes significantly to the pool of floodplain carbon. The fraction of N derived from shale may be even higher based on the high C:N ratio (relatively low N content) in the light fractions compared to the heavy fraction. The samples were collected over a range of typical floodplain environments within the fairly narrow valley (200 m wide) of the East River lower montane site and thus represent a reasonable estimate of the entire shale-derived pool at this site. While we found no other estimates of the contribution of ancient OC to floodplain sediments in the literature, similar proportions of ancient OC have been observed in other freshwater environments, including sediments of a perialpine lake (30%; Blattmann et al., 2019) and Amazon river bed sediments (23–62%; Bouchez et al., 2010). On a global scale, the contribution of ancient OC to riverine OC export to oceans is poorly constrained and ranges widely across different environments; however, Galy et al. (2015) estimated a global flux of 43 Mt C/year for petrogenic carbon exported to oceans, representing approximately 22% of the total carbon flux.

4.3. Evidence of Shale Weathering From Carbon Spectroscopy

Carbon NEXAFS spectroscopy on the shale samples (Table 4 and Figure 9) provide evidence for an increase in carbonate concentration during in situ shale weathering with little impact on OC content. While OC loss during in situ shale weathering has been observed in OC-rich (5–20% OC) black shales, it is generally

Table 3
Extractable Organic Carbon (OC_{ext}) Concentrations (Normalized Per Gram of Dry Sediment), $\Delta^{14}C$, and SUVA Values

	HCl		NaCl whole			PP whole	PP-SPE			PP >1 kDa	
Location	Depth (cm)	OC_{ext} (mg/g)	OC_{ext} (mg/g)	$\Delta^{14}C$ (‰)	SUVA (L/mg m)	OC_{ext} (mg/g)	OC_{ext} (mg/g)	$\Delta^{14}C$ (‰)	SUVA (L/mg m)	OC_{ext} (mg/g)	$\Delta^{14}C$ (‰)
MO-cut bank	15–30	1.37	0.207	NA	1.87	3.35	0.371	NA	6.41	1.13	NA
	50–70	0.798	0.045	NA	1.25	1.33	0.240	NA	5.53	0.725	NA
MO-middle	15–30	1.77	0.166	−7.2 ± 4.2	2.73	5.11	0.442	0.1 ± 3.3	5.65	1.19	−115.2 ± 2.9
	45–60	0.429	0.039	−344.8 ± 3.6	0.84	1.67	0.250	−144.7 ± 2.2	5.85	0.745	−457.4 ± 1.1
MO-point bar	15–26	1.39	0.240	NA	2.11	4.68	0.637	NA	6.60	1.70	NA
	41–56	0.391	0.047	NA	1.82	1.68	0.219	NA	6.50	0.539	NA
	71–91	0.310	0.054	NA	1.94	1.36	0.205	NA	7.42	0.441	NA
MO-wetland	15–30	0.633	0.041	NA	2.74	2.73	0.298	NA	6.43	1.16	NA
	30–45	0.418	0.032	NA	1.06	1.98	0.338	NA	5.29	0.887	NA
MC-cut bank	29–43	0.546	0.059	−71.1 ± 2.0	2.56	1.71	0.230	−34.7 ± 3.2	5.47	0.697	−385.7 ± 1.6
MC-middle	29–47	0.876	0.053	−134.3 ± 3.4	2.50	2.42	0.455	−69.0 ± 2.9	4.82	0.240	−341.7 ± 1.9
	80–90	0.732	0.079	−92.5 ± 2.5	3.66	2.33	0.357	−68.0 ± 2.5	5.78	0.955	−331.8 ± 1.7
MC-point bar	19–47	0.196	0.028	NA	1.53	0.588	0.118	−109.9 ± 3.8	6.00	0.132	−557.0 ± 1.6
	47–72	0.181	0.033	NA	1.13	0.638	0.104	NA	6.68	0.147	NA
	72–108	0.014	0.027	NA	1.11	0.499	0.098	NA	6.86	0.057	NA

Note. NA = data not available.

preceded by pyrite loss (Petsch et al., 2000; Petsch, Smernik, et al., 2001; Wildman et al., 2004) and the extent of OC loss can vary depending on the kerogen type (Petsch et al., 2000). Therefore, the minimal OC loss observed in our study may be due to the lower OC concentration, differences in the kerogen type, or a lower extent of pyrite oxidation. In floodplain sediments, the STXM data show small patches of carbon <1 μm, often less than 500 nm, in a matrix of carbon poor minerals (Figure S7), suggesting that the majority of the carbon spectra were from mineral associated carbon. The high aromaticity and other spectral features of the floodplain spectra are similar to the spectra of shale C, although with strong evidence for oxidative processing as seen in the increase in functionalized aromatics and carboxylic groups. Similar results, including an increase in the O/C ratio and an increase in C=C and C=O bonds, have been observed during oxidative weathering of black shales (Petsch et al., 2000; Petsch, Smernik, et al., 2001; Wildman et al., 2004) and during weathering of kerogen in soils developed on shale bedrock (Longbottom & Hockaday, 2019). The lower carbonate content in the floodplain samples suggests that inorganic C is leached from particles in the floodplain, as would be expected in the more frequently saturated environment. Bulk sediment IC concentrations (Figure S2) in MC-cut bank and MC-middle samples are very low (<0.1%) with slightly higher concentrations observed in deeper regions of MC-middle (0.2–0.6%), consistent with the STXM data. Higher IC concentrations (0.5–1.3%) are observed in the point bar locations (MC and MO) and wetland location of MO.

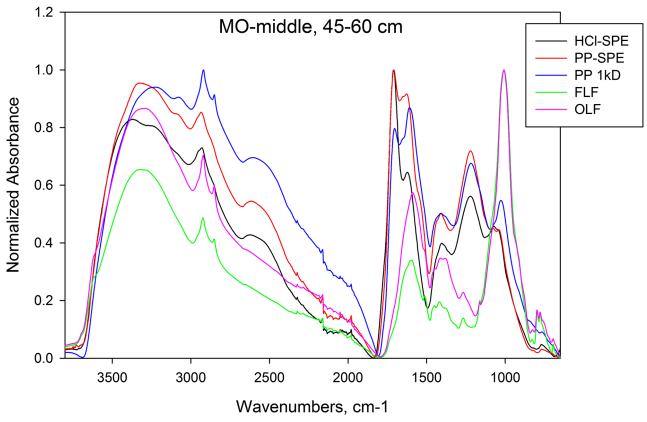

Figure 8. Example FTIR spectra from OC isolated by extraction (HCl-SPE, PP-SPE, and PP >1 kDa) and density fractionations (FLF, OLF). All data are from sample MO-middle, 45–60 cm.

The differences in organic functional groups in the floodplain particles compared to shale could be due to the direct alteration of shale-derived OC and/or the addition of plant/microbially derived compounds as coatings on the particles. Some evidence of microbially derived compounds was observed in the STXM data, namely, in particle 4 of MC-middle (Table 4 and supporting information). This spectrum was from a relatively large (>1 μm) spot of concentrated C. We propose that there is a weathering continuum from pristine to weathered shale, with an increase in carbonate and minimal changes in organics, followed by continued weathering of shale particles deposited in the floodplain, with leaching loss of carbonate and functionalization of OC through oxidative processes and the addition of microbially processed modern OC.

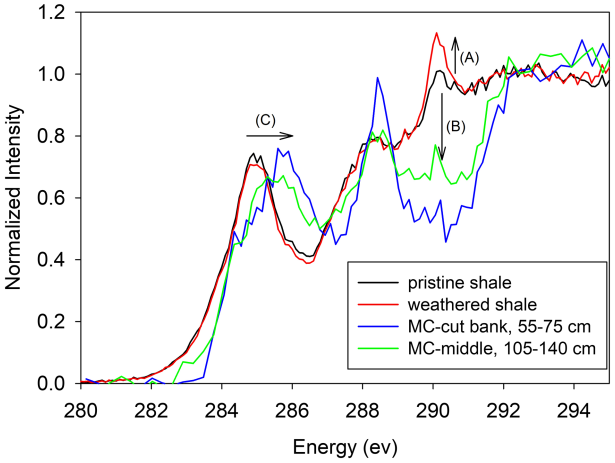

Figure 9. Example carbon spectra for weathered and pristine shale and floodplain sediments showing a shale weathering continuum, where (a) denotes an increase in carbonates during in situ shale weathering (i.e., pristine versus weathered shale), (b) denotes leaching loss of carbonates from shale samples to floodplain sediments, and (c) denotes an increase in functionalized carbonyl groups (oxidation) in floodplain sediments compared to shale.

4.4. Possible Role of Ancient OC in OLF Samples

Golchin et al. (1997, 1994) proposed a model for soil OC decomposition in which the average state of decomposition proceeds from FLF to OLF to HF. A greater state of decomposition is typically evidenced by lower C/N, higher $\delta^{13}C$, and lower $\Delta^{14}C$ values. However, Wagai et al. (2009) examined a wide range of data from the literature and found no consistent difference in these properties between FLF and OLF samples. Similarly, in a study of 12 different European soils, Schrumpf et al. (2013) noted that there was no consistent shift in C/N and $\delta^{13}C$ from FLF to OLF, but did observe that OLF was consistently older. In our study, we observe a consistent shift in C/N ratios and $\Delta^{14}C$ values across all three fractions and consistently lower $\delta^{13}C$ values in FLF samples. This observation is consistent with an increase in the average state of decomposition from FLF to OLF to HF. However, as discussed above, the differences in these values between the FLF and HF likely reflects two different sources of OC in the system, namely, (1) vegetative-derived OC from riparian zone vegetation (litter and root fragments) and/or alluvial deposition of upstream vegetative matter which makes up the entire FLF and (2) shale-derived OC, which makes up a large proportion of the HF.

The $\Delta^{14}C$ values for the OLF samples in our study are significantly lower than what was observed in the FLF samples, corresponding to ^{14}C ages up to 3,375 years B.P. It is difficult to determine whether this represents aging of relatively modern plant-derived OC (i.e., through occlusion within aggregates or other weak associations with mineral particles) or a mixture of fresh OC and ancient shale-derived OC. FTIR data indicate that the OLF is chemically very similar to the FLF; however, there is a shift in $\delta^{13}C$ and C/N ratios between the two fractions which suggests that there may be some small differences in chemistry and/or origin of the OC in these two fractions. A closer examination of the relationship between the C/N ratio and $\Delta^{14}C$ values (Figure 6d) shows a strong negative correlation between these two parameters within the OLF. In other words, the OLF sample with the highest C/N ratio (37.6 ± 0.5), which is typical of relatively unaltered vegetative debris, has the lowest $\Delta^{14}C$ value (−348.6‰), while the samples with the lowest C/N ratio (20.3–20.7), which is indicative of more microbially processed OC, have the highest $\Delta^{14}C$ values (4.5–28.2‰). Smaller OC particles are generally isolated from the OLF compared to the FLF, with few recognizable plant detrital

Table 4
Fitting Results From Carbon Spectra of Shale Samples and Floodplain Sediments

	Bulk C NEXAFS of shale core samples					STXM spectra of floodplain sediments							
	Hillslope		GRO			MC-cut (55–75 cm)		MC-mid (105–140 cm)				Average	
Functionality	Pristine	Weathered	Top	Middle	Bottom	Particle 1	Particle 2	Particle 1	Particle 2	Particle 3	Particle 4	Shale	Floodplain[a]
Quinone	7%	7%	8%	8%	8%	4%	2%	1%	4%	5%	0%	7.6 ± 0.6%	3.2 ± 1.6%
Aromatic (H/alkylated)	19%	19%	17%	18%	18%	16%	17%	14%	17%	17%	0%	18.3 ± 0.9%	16.2 ± 1.1%
Functionalized aromatic (carbonyl)	12%	11%	12%	12%	12%	28%	20%	26%	25%	22%	0%	11.8 ± 0.3%	24.2 ± 3.2%
Aromatic (C–OH)/ aliphatic	13%	13%	12%	12%	12%	8%	18%	13%	11%	13%	0%	12.1 ± 0.5%	12.3 ± 3.7%
Carboxylic	14%	14%	15%	14%	14%	23%	15%	20%	17%	17%	48%	14.5 ± 0.5%	18.3 ± 3.2%
Alkyl–OH	11%	10%	9%	9%	9%	11%	16%	16%	12%	13%	28%	9.7 ± 0.9%	13.5 ± 2.0%
Carbonate	23%	26%	27%	27%	28%	10%	13%	10%	13%	15%	23%	26.1 ± 1.8%	12.3 ± 2.1%

[a]Particle 4 from the MC-middle sample is excluded from the averages due to the distinctly different character of that particle.

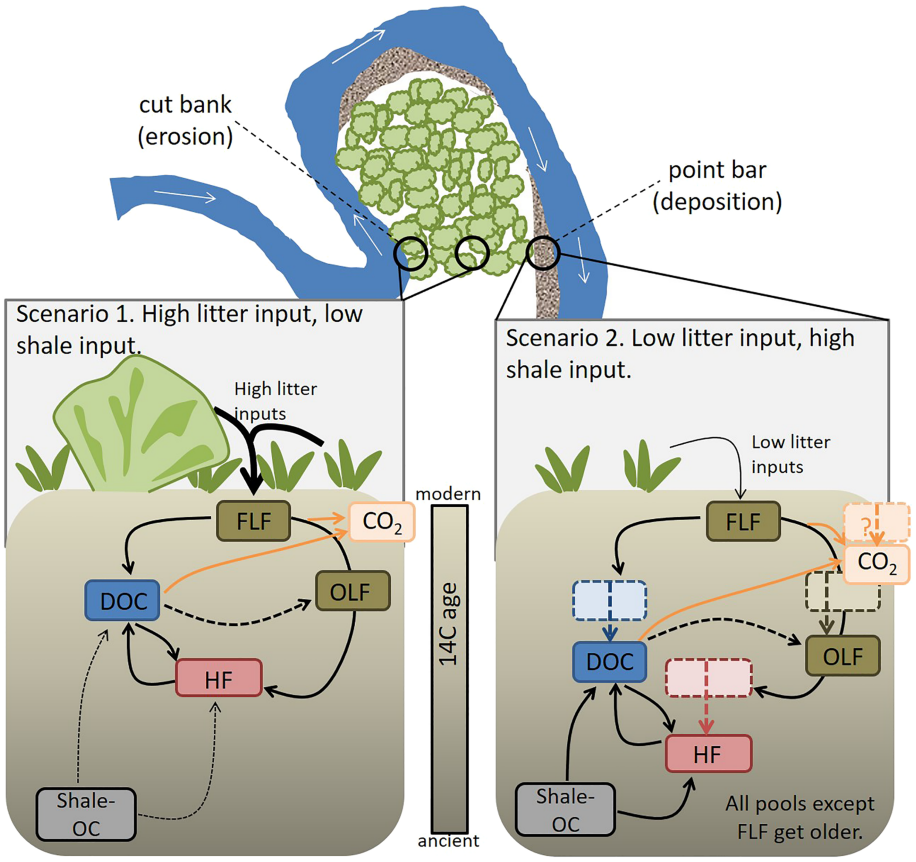

Figure 10. Conceptual diagram showing two scenarios: (1) high litter input with low shale input and (2) low litter input with high shale input. Scenario 1 is emblematic of regions of the floodplain with more extensive soil development (e.g., cut bank and middle of the meander) and nonshale systems, where OC is derived primarily from plant detritus and the ^{14}C age is controlled by occlusion of litter fragments in aggregates (OLF), which physically protects it from degradation, and mineral protection of processed OC (e.g., partially oxidized and degraded) through adsorption or occlusion within mineral particles (HF). Scenario 2 (point bar) represents a shale-rich environment with low litter inputs, where the OC is derived from both shale and plant litter and ^{14}C age of all pools except for FLF is lowered by the presence of shale-derived carbon. The role of shale-derived OC in CO_2 release is currently unknown.

structures. This fraction can contain fungal spores, char (pyrogenic carbon), and microbial residues in addition to partially decomposed plant detritus (Baisden et al., 2002; Brodowski et al., 2006; Golchin et al., 1994; Heckman et al., 2014; Wagai et al., 2008; Wagai et al., 2009). Wagai et al. (2009) proposed a new model in which this fraction (m-LF in their paper, equivalent to OLF in this paper) is composed of a combination of partially decomposed plant-detritus occluded by mineral particles with the assistance of microbial residues and less decomposed biomolecules or char which retain their original chemical composition. This model may help explain the negative correlation observed between OLF C/N and $\Delta^{14}C$, where high C/N, low $\Delta^{14}C$ samples represent physically protected plant detritus, while low C/N, high $\Delta^{14}C$ represents relatively young, but more decomposed plant-detritus. Given that the OLF is likely composed of a mixture of different types of materials, it is certainly possible that shale-derived OC, which has been chemically and microbially processed and released from the shale particles, has made its way into this fraction. The $\Delta^{14}C$ values observed in the OLF correspond to a fraction modern of 0.66–1.04, with most samples falling in the 0.83–1.03 range. Therefore, a maximum of 34% of the carbon in the OLF may be derived from shale, with 7–17% being more typical.

4.5. Mobility of Shale-Derived OC

Measurements of $\Delta^{14}C$ on extracted OC can provide some insight into the mobility and associations of shale-derived and modern OC in floodplain sediments. We use the NaCl-extractable fraction as a proxy for highly

mobile, soluble OC. The pyrophosphate-extractable OC represents OC stabilized through binding to mineral surfaces via ligand exchange, metal complexation, and cation-bridging (Pansu & Gautheyrou, 2006). The $\Delta^{14}C$ values of the PP-SPE fraction of the OC, which is soluble at pH 2, range from −144.7 to 0.1‰, and are similar to the values observed in the OLF (Figure 7). The PP >1-kDa fraction, which is insoluble in acid, is much older, with $\Delta^{14}C$ values (−557.0 to −115.2‰) that fall between the OLF and HF, suggesting that this fraction has a much larger contribution from shale-derived OC. Somewhat surprisingly, the NaCl whole samples have $\Delta^{14}C$ values that are slightly, but consistently, lower than the PP-SPE values ($\Delta^{14}C$ of −344.8 to −7.2‰). It is unknown whether the lower $\Delta^{14}C$ values in the NaCl fraction are due to real differences between water soluble (NaCl extracts) and metal-complexed (soluble at pH 2) pools of OC or whether this is an artifact of the SPE isolation procedure, which may induce a bias toward molecules that bind to the SPE resin. The recovery of OC during the SPE isolation procedure of PP extracts ranged from 21 to 40%. In either case, the depleted $\Delta^{14}C$ values observed in the NaCl extracts suggest that ancient shale-derived OC can be mobilized to the dissolved pool and may be an important source of dissolved organic carbon in the floodplain. The metal-complexed fraction of the OC (i.e., PP-extractable pool) may become mobilized under reducing conditions when Fe(III) oxides are solubilized. Root exudates (e.g., oxalic acid) may also promote the release of metal-complexed and mineral-bound carbon to the solution phase (Keiluweit et al., 2015). Reducing conditions can occur in permanently saturated locations, such as in the oxbow wetland, where dissolved oxygen is limited. There may be a seasonal component to the release of metal-complexed OC as well due to the inundation of the floodplain during spring snowmelt, seasonal temperature changes, and seasonal changes in plant growth and senescence.

4.6. Conclusions and Conceptual Model of Organic Carbon Cycling in Shale-Rich Environments

Through the use of radiocarbon measurements, we found that a large fraction (23–34%) of OC in floodplain sediments is derived from shale. Evidence of shale-derived OC is observed in all pools of sediment-OC, with the exception of the FLF pool. This includes pools which are considered to be relatively mobile (e.g., NaCl-extractable) and susceptible to microbial processing (e.g., PP-extractable and OLF) under changing biogeochemical conditions in the hydrologically dynamic floodplain environment. Figure 10 shows a conceptual diagram illustrating the OC cycle in two scenarios: (1) system with high litter inputs and low shale input and (2) system with low litter inputs and high shale inputs. Scenario (1) is representative of floodplain regions with more extensive soil development (e.g., cut bank and middle of the meander) and is also typical of nonshale soils or sediments where ^{14}C age is primarily controlled by physical protection and adsorption to or occlusion by mineral particles (e.g., according to the models of Kleber (2010), Kleber et al. (2011), and Schmidt et al. (2011)), with little influence of shale-derived OC. It should be noted that high litter inputs can be caused by both riparian zone vegetation and deposition of river-transported plant debris. By contrast, regions with lower vegetative inputs and resulting low sediment OC values, such as the point bar location of an active meander (depositional environment with minimal soil development), shale-derived OC makes up a much larger fraction of OC in all pools. While the contribution of shale-derived OC to CO_2 mineralization and export is currently unknown in this system, the observation of shale-derived OC in carbon pools which we consider to be actively cycling suggests that this topic warrants further research. This study joins a mounting body of evidence of the important contribution of ancient rock-derived OC in modern riverine systems (Blair et al., 2003; Caraco et al., 2010; Goñi et al., 2005; Komada et al., 2004; Komada et al., 2005; Leithold et al., 2006; Raymond & Bauer, 2001a, 2001b). These inputs are not included in current global C models, but may play a significant role in the global C cycle through export of ancient OC to oceans, which is estimated at 22% globally (Galy et al., 2015), and mineralization of ancient OC in riverine systems with extensive floodplains (e.g., Bouchez et al., 2010; Galy et al., 2008). Furthermore, evidence of shale-OC release from floodplain sediments suggests that shale weathering in the floodplain may be a significant source of other shale-associated elements, including growth-limiting nutrients (e.g., N) and toxic elements (e.g., As, Se, U).

Acknowledgments
The authors thank Scott Fendorf, Christian Dewey, and Hannah Naughton (Stanford University) for assistance with sediment sampling and Natalie Penado and Amrita Bhattacharyya (LBL) for assistance with sediment sample processing in the laboratory. Benjamin Gilbert and John Christensen (LBL) provided the shale samples. We thank Joel Rowland and Thomas Blattmann for helpful reviews. This work was supported by the Watershed Function Scientific Focus Area funded by the U.S. Department of Energy, Office of Science, Office of Biological and Environmental Research under contract DE-AC02-05CH11231 with Lawrence Berkeley National Laboratory. M.K. and C.A. were supported by the Department of Energy, Office of Biological and Environmental Research, Subsurface Biosphere Research program (award DE-SC0016544). Research described in this paper was performed at the Canadian Light Source, which is supported by the Canada Foundation for Innovation, Natural Sciences and Engineering Research Council of Canada, the University of Saskatchewan, the Government of Saskatchewan, Western Economic Diversification Canada, the National Research Council Canada, and the Canadian Institutes of Health Research. Radiocarbon analysis was supported in part by the Radiocarbon Collaborative, which is jointly sponsored by the USDA Forest Service Northern Research Station, the KCCAMS Facility at UC Irvine, and Michigan Technological University. The data used in this work are available online at the ESS-DIVE database (Fox et al., 2019). Data include sediment sieving data, sediment extraction data, carbon and nitrogen contents and carbon isotopes (^{14}C and ^{13}C) of whole sediment and sediment density fractions, and FTIR, UV-Vis, C NEXAFS, and STXM data.

References

Baes, A. U., & Bloom, P. R. (1989). Diffuse reflectance and transmission Fourier transform infrared (DRIFT) spectroscopy of humic and fulvic acids. *Soil Science Society of America Journal*, *53*, 695–700.

Baisden, W. T., Amundson, R., Brenner, D. L., Cook, A. C., Kendall, C., & Harden, J. W. (2002). A multiisotope C and N modeling analysis of soil organic matter turnover and transport as a function of soil depth in a California annual grassland soil chronosequence. *Global Biogeochemical Cycles*, *16*(4), 1135. https://doi.org/10.1029/2001GB001823

Baisden, W. T., Amundson, R., Cook, A. C., & Brenner, D. L. (2002). Turnover and storage of C and N in five density fractions from California annual grassland surface soils. *Global Biogeochemical Cycles*, *16*(4), 1117. https://doi.org/10.1029/2001GB001822

Berner, R. A. (1987). Models for carbon and sulfur cycles and atmospheric oxygen: Application to Paleozoic geologic history. *American Journal of Science*, *287*, 177–196.

Blair, N. E., Leithold, E. L., Ford, S. T., Peeler, K. A., Holmes, J. C., & Perkey, D. W. (2003). The persistence of memory: The fate of ancient sedimentary organic carbon in a modern sedimentary system. *Geochimica et Cosmochimica Acta*, *67*, 63–73.

Blattmann, T. M., Wessels, M., McIntyre, C. P., & Eglinton, T. I. (2019). Petrogenic organic carbon retention in terrestrial basins: A case study from perialpine Lake Constance. *Chemical Geology*, *503*, 52–60.

Bouchez, J., Beyssac, O., Galy, V., Gaillardet, J., France-Lanord, C., Maurice, L., & Moreira-Turcq, P. (2010). Oxidation of petrogenic organic carbon in the Amazon floodplain as a source of atmospheric CO_2. *Geology*, *38*, 255–258.

Brandes, J. A., Wirick, S., & Jacobsen, C. (2010). Carbon K-edge spectra of carbonate minerals. *Journal of Synchrotron Radiation*, *17*(5), 676–682. https://doi.org/10.1107/S0909049510020029

Brodowski, S., John, B., Flessa, H., & Amelung, W. (2006). Aggregate-occluded black carbon in soil. *European Journal of Soil Science*, *57*, 539–546.

Caraco, N., Bauer, J. E., Cole, J. J., Petsch, S., & Raymond, P. (2010). Millennial-aged organic carbon subsidies to a modern river food web. *Ecology*, *91*(8), 2385–2393. https://doi.org/10.1890/09-0330.1

Chigira, M., & Oyama, T. (2000). Mechanism and effect of chemical weathering of sedimentary rocks. *Engineering Geology*, *55*, 3–14.

Cody, G. D., Ade, H., Wirick, S., Mitchell, G. D., & Davis, A. (1998). Determination of chemical-structural changes in vitrinite accompanying luminescence alteration using C-NEXAFS analysis. *Organic Geochemistry*, *28*, 441–455.

Dittmar, T., Koch, B., Hertkorn, N., & Kattner, G. (2008). A simple and efficient method for the solid-phase extraction of dissolved organic matter (SPE-DOM) from seawater. *Limnology and Oceanography: Methods*, *6*, 230–235.

Dwivedi, D., Steefel, C., Arora, B., Newcomer, M., Moulton, J. D., Dafflon, B., et al. (2018). Geochemical exports to river from the intra-meander hyporheic zone under transient hydrologica conditions: East River mountainous watershed, Colorado. *Water Resources Research*, *54*, 8456–8477. https://doi.org/10.1029/2018WR023377

Evangelou, V. P., & Zhang, Y. L. (1995). A review: Pyrite oxidation mechanisms and acid mine drainage prevention. *Critical Reviews in Environmental Science and Technology*, *25*, 141–199.

Falco, N., Wainwright, H., Dafflon, B., Léger, E., Peterson, J., Steltzer, H., et al. (2019). Investigating microtopographic and soil controls on a mountainous meadow plant community using high-resolution remote sensing and surface geophysical data. *Journal of Geophysical Research: Biogeosciences*, *124*, 1618–1636. https://doi.org/10.1029/2018JG004394

Fox, P. M., Bill, M., Heckman, K., Conrad, M., Anderson, C., Keiluweit, M., & Nico, P. S. (2019). *Geochemical characterization of floodplain sediments from Meander C and O in the East River Watershed*. CO, USA: Watershed Function SFA. https://doi.org/10.21952/WTR/1572186

Fox, P. M., Nico, P. S., Tfaily, M. M., Heckman, K., & Davis, J. A. (2017). Characterization of natural organic matter in low-carbon sediments: Extraction and analytical approaches. *Organic Geochemistry*, *114*, 12–22.

Francis, J. T., & Hitchcock, A. P. (1992). Inner-shell spectroscopy of para-benzoquinone, hydroquinone, and phenol-distinguishing quinoid and benzenoid structures. *Journal of Physical Chemistry*, *96*, 6598–6610.

Galy, V., Beyssac, O., France-Lanord, C., & Eglinton, T. (2008). Recycling of graphite during Himalayan erosion: A geological stabilization of carbon in the crust. *Science*, *322*(5903), 943–945. https://doi.org/10.1126/science.1161408

Galy, V., Peucker-Ehrenbrink, B., & Eglinton, T. (2015). Global carbon export from the terrestrial biosphere controlled by erosion. *Nature*, *521*, 204.

Gaskill, D. L., Mutschler, F. E., Kramer, J. H., Thomas, J. A., & Zahony, S. G. (1991). Geologic map of the Gothic quadrangle, Gunnison County, Colorado, Geologic Quadrangle, US Geological Survey.

Golchin, A., Baldock, J., & Oades, J. (1997). *A model linking organic matter decomposition, chemistry, and aggregate dynamics. Soil processes and the carbon cycle* (pp. 245–266). Boca Raton: CRC Press.

Golchin, A., Oades, J., Skjemstad, J., & Clarke, P. (1994). Study of free and occluded particulate organic matter in soils by solid state ^{13}C Cp/MAS NMR spectroscopy and scanning electron microscopy. *Soil Research*, *32*, 285–309.

Goñi, M. A., Yunker, M. B., Macdonald, R. W., & Eglinton, T. I. (2005). The supply and preservation of ancient and modern components of organic carbon in the Canadian Beaufort Shelf of the Arctic Ocean. *Marine Chemistry*, *93*, 53–73.

Graf-Rosenfellner, M., Cierjacks, A., Kleinschmit, B., & Lang, F. (2016). Soil formation and its implications for stabilization of soil organic matter in the riparian zone. *Catena*, *139*, 9–18.

Gurwick, N. P., McCorkle, D. M., Groffman, P. M., Gold, A. J., Kellogg, D. Q., & Seitz-Rundlett, P. (2008). Mineralization of ancient carbon in the subsurface of riparian forests. *Journal of Geophysical Research*, *113*, G02021. https://doi.org/10.1029/2007JG000482

Heckman, K., Throckmorton, H., Clingensmith, C., González Vila, F. J., Horwath, W. R., Knicker, H., & Rasmussen, C. (2014). Factors affecting the molecular structure and mean residence time of occluded organics in a lithosequence of soils under ponderosa pine. *Soil Biology and Biochemistry*, *77*, 1–11.

Hemingway, J. D., Hilton, R. G., Hovius, N., Eglinton, T. I., Haghipour, N., Wacker, L., et al. (2018). Microbial oxidation of lithospheric organic carbon in rapidly eroding tropical mountain soils. *Science*, *360*(6385), 209–212. https://doi.org/10.1126/science.aao6463

Hicks Pries, C. E., Castanha, C., Porras, R. C., & Torn, M. S. (2017). The whole-soil carbon flux in response to warming. *Science*, *355*(6332), 1420–1423. https://doi.org/10.1126/science.aal1319

Hitchcock, A. P., Urquhart, S. G., & Rightor, E. G. (1992). Inner-shell spectroscopy of benzaldehyde, terephthalaldehyde, ethyl benzoate, terephthaloyl chloride, and phosgene: Models for core excitation of poly (ethylene-terephthalate). *Journal of Physical Chemistry*, *96*, 8736–8750.

Houlton, B. Z., Morford, S. L., & Dahlgren, R. A. (2018). Convergent evidence for widespread rock nitrogen sources in Earth's surface environment. *Science*, *360*(6384), 58–62. https://doi.org/10.1126/science.aan4399

Hubbard, S. S., Williams, K. H., Agarwal, D., Banfield, J., Beller, H., Bouskill, N., et al. (2018). The East River, Colorado, Watershed: A mountainous community testbed for improving predictive understanding of multiscale hydrological–biogeochemical dynamics. *Vadose Zone Journal*, *17*.

Kao, S.-J., & Liu, K.-K. (1996). Particulate organic carbon export from a subtropical mountainous river (Lanyang Hsi) in Taiwan. *Limnology and Oceanography*, *41*, 1749–1757.

Kao, S.-J., Hilton, R. G., Selvaraj, K., Dai, M., Zehetner, F., Huang, J.-C., et al. (2014). Preservation of terrestrial organic carbon in marine sediments offshore Taiwan: mountain building and atmospheric carbon dioxide sequestration. *Earth Surface Dynamics*, *2*(1), 127–139. https://doi.org/10.5194/esurf-2-127-2014

Keiluweit, M., Bougoure, J. J., Nico, P. S., Pett-Ridge, J., Weber, P. K., & Kleber, M. (2015). Mineral protection of soil carbon counteracted by root exudates. *Nature Climate Change*, *5*, 588.

Kleber, M. (2010). What is recalcitrant soil organic matter? *Environmental Chemistry*, *7*, 320–332.

Kleber, M., Nico, P. S., Plante, A., Filley, T., Kramer, M., Swanston, C., & Sollins, P. (2011). Old and stable soil organic matter is not necessarily chemically recalcitrant: Implications for modeling concepts and temperature sensitivity. *Global Change Biology*, *17*, 1097–1107.

Komada, T., Druffel, E. R. M., & Hwang, J. (2005). Sedimentary rocks as sources of ancient organic carbon to the ocean: An investigation through $\Delta^{14}C$ and $\delta^{13}C$ signatures of organic compound classes. *Global Biogeochemical Cycles*, *19*, GB2017. https://doi.org/10.1029/2004GB002347

Komada, T., Druffel, E. R. M., & Trumbore, S. E. (2004). Oceanic export of relict carbon by small mountainous rivers. *Geophysical Research Letters*, *31*, L07504. https://doi.org/10.1029/2004GL019512

Lalonde, K., Mucci, A., Ouellet, A., & Gelinas, Y. (2012). Preservation of organic matter in sediments promoted by iron. *Nature*, *483*(7388), 198–200. https://doi.org/10.1038/nature10855

Leithold, E. L., Blair, N. E., & Perkey, D. W. (2006). Geomorphologic controls on the age of particulate organic carbon from small mountainous and upland rivers. *Global Biogeochemical Cycles*, *20*, GB3022. https://doi.org/10.1029/2005GB002677

Leythaeuser, D. (1973). Effects of weathering on organic matter in shales. *Geochimica et Cosmochimica Acta*, *37*, 113–120.

Littke, R., Klussmann, U., Krooss, B., & Leythaeuser, D. (1991). Quantification of loss of calcite, pyrite, and organic matter due to weathering of Toarcian black shales and effects on kerogen and bitumen characteristics. *Geochimica et Cosmochimica Acta*, *55*, 3369–3378.

Loeppert, R. H., & Inskeep, W. P. (1996). Iron. In D. L. Sparks (Ed.), *Methods of soil analysis*, *Part* (Vol. 3, pp. 639–664). Madison, WI: Chemical methods. ASA and SSSA.

Longbottom, T. L., & Hockaday, W. C. (2019). Molecular and isotopic composition of modern soils derived from kerogen-rich bedrock and implications for the global C cycle. *Biogeochemistry*, *143*, 239–255.

Ma, Y., Chen, C. T., Meigs, G., Randall, K., & Sette, F. (1991). High-resolution K-shell photoabsorption measurements of simple molecules. *Physical Review A*, *44*, 1848–1858.

McFarlane, K. J., Torn, M. S., Hanson, P. J., Porras, R. C., Swanston, C. W., Callaham, M. A., & Guilderson, T. P. (2013). Comparison of soil organic matter dynamics at five temperate deciduous forests with physical fractionation and radiocarbon measurements. *Biogeochemistry*, *112*, 457–476.

Meybeck, M. (1993). Riverine transport of atmospheric carbon: Sources, global typology and budget. *Water, Air, and Soil Pollution*, *70*, 443–463.

Morrison, S. J., Goodknight, C. S., Tigar, A. D., Bush, R. P., & Gil, A. (2012). Naturally occurring contamination in the Mancos Shale. *Environmental Science & Technology*, *46*(3), 1379–1387. https://doi.org/10.1021/es203211z

Pansu, M., & Gautheyrou, J. (2006). *Mineralogical separation by selective dissolution, Handbook of soil analysis: Mineralogical, organic, and inorganic methods* (pp. 167–219). Berlin, Heidelberg: Springer.

Petsch, S. (2017). Kerogen. In W. M. White (Ed.), *Encyclopedia of geochemistry: A comprehensive reference source on the chemistry of the Earth* (pp. 1–5). Cham: Springer International Publishing.

Petsch, S. T., Berner, R. A., & Eglinton, T. I. (2000). A field study of the chemical weathering of ancient sedimentary organic matter. *Organic Geochemistry*, *31*, 475–487.

Petsch, S. T., Eglinton, T. I., & Edwards, K. J. (2001). ^{14}C-dead living biomass: Evidence for microbial assimilation of ancient organic carbon during shale weathering. *Science*, *292*(5519), 1127–1131. https://doi.org/10.1126/science.1058332

Petsch, S. T., Smernik, R. J., Eglinton, T. I., & Oades, J. M. (2001). A solid state ^{13}C-NMR study of kerogen degradation during black shale weathering. *Geochimica et Cosmochimica Acta*, *65*, 1867–1882.

Ramnarine, R., Voroney, R., Wagner-Riddle, C., & Dunfield, K. (2011). Carbonate removal by acid fumigation for measuring the $\delta^{13}C$ of soil organic carbon. *Canadian Journal of Soil Science*, *91*, 247–250.

Ravel, B., & Newville, M. (2005). ATHENA, ARTEMIS, HEPHAESTUS: Data analysis for X-ray absorption spectroscopy using IFEFFIT. *Journal of Synchrotron Radiation*, *12*(Pt 4), 537–541. https://doi.org/10.1107/S0909049505012719

Raymond, P. A., & Bauer, J. E. (2001a). Riverine export of aged terrestrial organic matter to the North Atlantic Ocean. *Nature*, *409*(6819), 497–500. https://doi.org/10.1038/35054034

Raymond, P. A., & Bauer, J. E. (2001b). Use of ^{14}C and ^{13}C natural abundances for evaluating riverine, estuarine, and coastal DOC and POC sources and cycling: A review and synthesis. *Organic Geochemistry*, *32*, 469–485.

Regier, T., Krochak, J., Sham, T., Hu, Y., Thompson, J., & Blyth, R. (2007). Performance and capabilities of the Canadian Dragon: The SGM beamline at the Canadian Light Source. *Nuclear Instruments and Methods in Physics Research Section A: Accelerators, Spectrometers, Detectors and Associated Equipment*, *582*, 93–95.

Schillawski, S., & Petsch, S. (2008). Release of biodegradable dissolved organic matter from ancient sedimentary rocks. *Global Biogeochemical Cycles*, *22*, GB3002. https://doi.org/10.1029/2007GB002980

Schmidt, M. W. I., Rumpel, C., & Kögel-Knabner, I. (1999). Evaluation of an ultrasonic dispersion procedure to isolate primary organomineral complexes from soils. *European Journal of Soil Science*, *50*, 87–94.

Schmidt, M. W. I., Torn, M. S., Abiven, S., Dittmar, R., Guggenberger, G., Janssens, I. A., et al. (2011). Persistence of soil organic matter as an ecosystem property. *Nature*, *478*(7367), 49–56. https://doi.org/10.1038/nature10386

Schrumpf, M., Kaiser, K., Guggenberger, G., Persson, T., Kögel-Knabner, I., & Schulze, E.-D. (2013). Storage and stability of organic carbon in soils as related to depth, occlusion within aggregates, and attachment to minerals. *Biogeosciences*, *10*, 1675–1691.

Southon, J. R., & Magana, A. L. (2010). A comparison of cellulose extraction and ABA pretreatment methods for AMS ^{14}C dating of ancient wood. *Radiocarbon*, *52*, 1371–1379.

Srdoc, D., Obelic, B., Horvatincic, N., & Sliepcevic, A. (1979). Measurement of the ^{14}C activity of the ANU sucrose secondary standard by means of the proportional counter technique. *Radiocarbon*, *21*, 321–328.

Stevenson, F. J. (1994). *Humus chemistry: Genesis, composition, reactions*. New York, USA: John Wiley & Sons.

Strawn, D., Doner, H., Zavarin, M., & McHugo, S. (2002). Microscale investigation into the geochemistry of arsenic, selenium, and iron in soil developed in pyritic shale materials. *Geoderma*, *108*, 237–257.

Stuiver, M., & Polach, H. A. (1977). Discussion reporting of ^{14}C data. *Radiocarbon*, *19*, 355–363.

Sutfin, N. A., Wohl, E. E., & Dwire, K. A. (2016). Banking carbon: A review of organic carbon storage and physical factors influencing retention in floodplains and riparian ecosystems. *Earth Surface Processes and Landforms*, *41*, 38–60.

Swanston, C. W., Torn, M. S., Hanson, P. J., Southon, J. R., Garten, C. T., Hanlon, E. M., & Ganio, L. (2005). Initial characterization of processes of soil carbon stabilization using forest stand-level radiocarbon enrichment. *Geoderma*, *128*, 52–62.

van der Voort, T. S., Mannu, U., Hagedorn, F., McIntyre, C., Walthert, L., Schleppi, P., et al. (2019). Dynamics of deep soil carbon–insights from 14C time series across a climatic gradient. *Biogeosciences*, *16*, 3233–3246.

Vogel, J. S., Southon, J. R., & Nelson, D. E. (1987). Catalyst and binder effects in the use of filamentous graphite for AMS. *Nuclear Instruments and Methods in Physics Research Section B: Beam Interactions with Materials and Atoms*, *29*, 50–56.

Vonk, J. E., Dickens, A. F., Giosan, L., Hussain, Z. A., Kim, B., Zipper, S. C., et al. (2016). Arctic Deltaic Lake Sediments As Recorders of Fluvial Organic Matter Deposition. *Frontiers in Earth Science*, *4*. https://doi.org/10.3389/feart.2016.00077

Wagai, R., & Mayer, L. M. (2007). Sorptive stabilization of organic matter in soils by hydrous iron oxides. *Geochimica et Cosmochimica Acta*, *71*, 25–35.

Wagai, R., Mayer, L. M., & Kitayama, K. (2009). Nature of the "occluded" low-density fraction in soil organic matter studies: A critical review. *Soil Science and Plant Nutrition*, *55*, 13–25.

Wagai, R., Mayer, L. M., Kitayama, K., & Knicker, H. (2008). Climate and parent material controls on organic matter storage in surface soils: A three-pool, density-separation approach. *Geoderma*, *147*, 23–33.

Wagai, R., Mayer, L. M., Kitayama, K., & Shirato, Y. (2011). Association of organic matter with iron and aluminum across a range of soils determined via selective dissolution techniques coupled with dissolved nitrogen analysis. *Biogeochemistry*, *112*(1-3), 95–109.

Wainwright, H., & Williams, K. (2017). LiDAR collection in August 2015 over the East River Watershed, Colorado, USA. [dataset] https://doi.org/10.21952/WTR/1412542

Wakeham, S., & Canuel, E. (2016). The nature of organic carbon in density-fractionated sediments in the Sacramento-San Joaquin River Delta (California). *Biogeosciences*, *13*, 567.

Weishaar, J. L., Aiken, G. R., Bergamaschi, B. A., Fram, M. S., Fujii, R., & Mopper, K. (2003). Evaluation of specific ultraviolet absorbance as an indicator of the chemical composition and reactivity of dissolved organic carbon. *Environmental Science & Technology*, *37*(20), 4702–4708. https://doi.org/10.1021/es030360x

Wildman, R. A., Berner, R. A., Petsch, S. T., Bolton, E. W., Eckert, J. O., Mok, U., & Evans, J. B. (2004). The weathering of sedimentary organic matter as a control on atmospheric O_2: I. Analysis of a black shale. *American Journal of Science*, *304*, 234–249.

Wohl, E., Dwire, K., Sutfin, N., Polvi, L., & Bazan, R. (2012). Mechanisms of carbon storage in mountainous headwater rivers. *Nature Communications*, *3*, 1263.

Zoppi, U., Crye, J., Song, Q., & Arjomand, A. (2007). Performance evaluation of the new AMS system at Accium BioSciences. *Radiocarbon*, *49*, 171–180.